

# 1 The Extra-Islet Pancreas Supports 2 Autoimmunity in Human Type 1 Diabetes

3  
4 Barlow, G.L.<sup>1,2,†</sup>, Schürch, C.M.<sup>2,4</sup>, Bhate, S.S.<sup>2</sup>, Phillips, D.<sup>2</sup>, Young, A.<sup>3,6,7</sup>, Dong, S.<sup>3,5</sup> Martinez, HA.<sup>1</sup>,  
5 Kaber, G.<sup>1</sup>, Nagy, N.<sup>1</sup>, Ramachandran S.<sup>1</sup>, Meng, J.<sup>1</sup>, Korpos E.<sup>9</sup> Bluestone, J.A.<sup>†,8</sup>, Nolan, G.P.<sup>†,2</sup>,  
6 Bollyky, P.L.<sup>†,‡,1</sup>

7  
8 † Corresponding Author

9 ‡ Lead Contact

10

## 11 **Affiliations:**

- 12 1. Division of Infectious Diseases and Geographic Medicine, Department of Medicine, Stanford  
13 University School of Medicine, Stanford, CA 94305, USA
- 14 2. Department of Pathology, Stanford University School of Medicine, Stanford, CA 94305, USA
- 15 3. Diabetes Center, University of California San Francisco, San Francisco, CA 94143, USA
- 16 4. Department of Pathology and Neuropathology, University Hospital and Comprehensive  
17 Cancer Center, Tübingen, Germany
- 18 5. Sean N. Parker Autoimmune Research Laboratory and Diabetes Center, University of  
19 California San Francisco, San Francisco, CA, USA
- 20 6. Huntsman Cancer Institute, University of Utah Health Sciences Center, Salt Lake City, UT  
21 84112, USA
- 22 7. Department of Pathology, University of Utah School of Medicine, Salt Lake City, UT 84112,  
23 USA
- 24 8. Sonoma Biotherapeutics, South San Francisco, CA 94080 USA
- 25 9. Institute of Physiological Chemistry and Pathobiochemistry and Cells-in-Motion Interfaculty  
26 Center, University of Muenster, Germany

27

28 Further information and requests for resources and reagents should be directed to and will be  
29 fulfilled by the lead contact, Paul Bollyky ([pbollyky@stanford.edu](mailto:pbollyky@stanford.edu)).

30

31

32

33

34

35

36 **Abstract**

37 In autoimmune Type 1 diabetes (T1D), immune cells infiltrate and destroy the islets of  
38 Langerhans — islands of endocrine tissue dispersed throughout the pancreas. However, the  
39 contribution of cellular programs outside islets to insulinitis is unclear. Here, using CO-Detection  
40 by indEXing (CODEX) tissue imaging and cadaveric pancreas samples, we simultaneously examine  
41 islet and extra-islet inflammation in human T1D. We identify four sub-states of inflamed islets  
42 characterized by the activation profiles of CD8<sup>+</sup>T cells enriched in islets relative to the surrounding  
43 tissue. We further find that the extra-islet space of lobules with extensive islet-infiltration differs  
44 from the extra-islet space of less infiltrated areas within the same tissue section. Finally, we  
45 identify lymphoid structures away from islets enriched in CD45RA<sup>+</sup> T cells — a population also  
46 enriched in one of the inflamed islet sub-states. Together, these data help define the  
47 coordination between islets and the extra-islet pancreas in the pathogenesis of human T1D.

48

49

50

51 **Keywords:** Type 1 Diabetes; Insulinitis; Autoimmunity; Multiplexed Imaging; CODEX; Systems  
52 Immunology; Tissue Architecture

## 53 Main

54 In Type 1 diabetes (T1D), insulin-producing  $\beta$ -cells are killed by islet-infiltrating immune cells in a  
55 process called “insulinitis”. T1D results in a critical requirement for exogenous insulin and affects  
56 over eight million individuals world-wide with an estimated 0.5 million new diagnoses each year<sup>1</sup>.

57 Recently, the first immunotherapy for delaying T1D onset, teplizumab (a human anti-CD3  
58 monoclonal antibody) was approved by the US Food and Drug Administration<sup>2</sup>. However, this  
59 treatment and other immunotherapies help only a small fraction of patients and are significantly  
60 less effective after patients progress to overt T1D<sup>3–9</sup>. A better understanding of T1D pathogenesis  
61 is essential to building on this progress.

62 One of the challenges of studying human T1D pathology is the availability of suitable tissue  
63 samples. Obtaining pancreatic biopsies raises the risk of surgical complications and the  
64 progressive nature of T1D would necessitate serial, longitudinal studies over time, which is  
65 prohibitive<sup>10</sup>. Fortunately, the Juvenile Diabetes Research Foundation (JDRF) Network for  
66 Pancreatic Organ Donors with Diabetes (nPOD) have provided human pancreatic tissues from  
67 cadaveric donors for this study<sup>11,12</sup>. nPOD has enabled substantial progress towards  
68 characterizing the pathology of human T1D<sup>13–17</sup>.

69 Our understanding of key features of human T1D pathology remains limited. Although the  
70 cellular composition of insulinitis, inflammation specifically of the islets, has been studied  
71 extensively, this has been done in separate studies looking at different tissue sections, prohibiting  
72 an understanding of how the numerous cellular programs in insulinitis are coordinated throughout  
73 disease. This was recently addressed using Imaging Mass Cytometry (IMC), which uncovered  
74 alterations in  $\beta$ -cell phenotypes, immune composition, vascular density, and basement  
75 membrane that accompany T1D<sup>18,19</sup>. However, these studies did not deeply phenotype islet-  
76 infiltrating CD8<sup>+</sup>T cells, believed to be major driver of  $\beta$ -cell elimination.

77 Recently, intriguing differences in the extra-islet spaces of T1D and healthy controls have been  
78 reported. First, the abundance of multiple types of immune cells outside islets are increased in  
79 T1D patients compared to non-T1D controls<sup>20–22</sup>. Second, HLA-DR expression is increased on  
80 ductal cells in T1D tissue donors, hinting at a functional link with CD4<sup>+</sup>T cells<sup>23</sup>. Third, peri-insulinitis,  
81 the accumulation of immune cells outside islets, is observed in tissues from patients with T1D<sup>24</sup>,  
82 indicating that not all T cells enter the pancreas directly via islet microvasculature<sup>25</sup>. Fourth, in  
83 human T1D, but less so in most animal models, islets in different regions of the pancreas are  
84 infiltrated at strikingly different rates for reasons that are unknown<sup>26</sup>. This suggests that the  
85 extra-islet compartment could be responsible by governing the targeting of islets. Finally, tertiary  
86 lymphoid structures (TLS) — dense aggregates of lymphoid cells indicative of local immune  
87 activation — are observed outside islets in T1D patients<sup>17</sup>.

88 In summary, analyzing both compartments simultaneously could help identify how these extra-  
89 islet factors influence islet pathogenesis. However, to date, multiplexed imaging studies have  
90 only examined islets. A comprehensive, spatially resolved cellular analysis of both compartments  
91 in T1D is lacking.

92 Here, we investigated the islet and extra-islet pancreas together. We used CO-Detection by  
93 indexing (CODEX) with an antibody panel targeting 54 antigens to samples from a cohort of T1D  
94 patients with insulinitis as well as non-T1D individuals with and without islet-specific  
95 autoantibodies (AA- and AA+ respectively) obtained through the JDRF nPOD program. We  
96 analyzed approximately 2000 islets and broad swaths of the extra-islet tissue to evaluate local  
97 and distal spatial architecture. We then used pseudotime analysis to characterize insulinitis sub-  
98 states based on the activation states of islet-infiltrating CD8<sup>+</sup>T cells. We further investigated the  
99 cellular changes in niches and lobules beyond islets. Our results implicate both the islet  
100 microenvironment and inflammation at distal sites within the pancreas in the progression of  
101 insulinitis.

## 102 Cohort curation, image acquisition, and cell annotation

103 The JDRF nPOD is a national registry of cadaveric pancreases donated by T1D patients that has  
104 transformed the ability of researchers to investigate the pathways underlying the progression of  
105 human T1D<sup>11,12</sup>. Insulinitis is present in only a small fraction of T1D cases, including those available  
106 from nPOD<sup>27,28</sup>. Although nPOD has close to 200 T1D cases, at the time of our study, nPOD had  
107 only 17 with documented insulinitis. Of these, triple-immunohistochemistry for Insulin, Glucagon,  
108 and CD3 was performed. T1D and AA+ cases that had CD3+ staining in islet or peri-islet spaces  
109 and tissue still available were selected for our study. The final cohort included two AA+ cases,  
110 eight T1D cases, and three non-T1D controls. Given that insulinitis is not detected in non-T1D  
111 cases<sup>29</sup>, the blocks from controls were selected randomly. The T1D cases varied in the time  
112 between diagnosis and death from 0 years (diagnosed at death) to 6 years (Figure 1.A, left). The  
113 causes of death were mostly unrelated to T1D complications (Supplemental Table 1). Therefore,  
114 the time since diagnosis is not a reflection of the aggressiveness of the individual's disease.

115 Large regions averaging 55 mm<sup>2</sup> were imaged with CODEX as previously described<sup>30-32</sup>. Regions  
116 were selected to capture islets and the surrounding region simultaneously (Figure 1.A, center  
117 and right). CellSeg was used to segment cell nuclei and quantify marker expression from CODEX  
118 images as previously described<sup>33</sup>. In total, our dataset consisted of 7.0x10<sup>6</sup> cells across all donors  
119 (ranging from 3.0x10<sup>5</sup> to 9.8x10<sup>5</sup> cells per donor). Twenty-one cell types were identified with  
120 Leiden clustering and manual merging and visualized using Uniform Manifold Approximation and  
121 Projection (UMAP) (Figure 1.B, Supplemental Table 2). Endocrine cells were manually gated from  
122 UMAP embeddings derived from Proinsulin, Glucagon, and Somatostatin to identify  $\beta$ -cells,  $\alpha$ -  
123 cells, and  $\delta$ -cells respectively. Immune cells were sub-clustered with the Leiden algorithm using  
124 immune-specific markers (Figure 1.C, Supplemental Table 2). To verify the accuracy of our  
125 annotations, we overlaid cell labels onto the original images (Supplemental Figure 1.A). Of note,  
126 we could not accurately identify macrophage subsets or distinguish dendritic cells from  
127 macrophages due to the panel design, complex combinations of co-expression, and the difficulty  
128 in segmenting and quantifying markers on myeloid populations due to their morphology.  
129 Therefore, we refer to this cluster as "macrophage/DCs" In addition, we identified a cell  
130 population that could not be definitively annotated, expressing high levels of CD45, CD69,  
131 Granzyme-B, and CD44, intermediate levels of CD16, S100A6, Galectin-3, and Hyaluronan, but  
132 not expressing CD3, CD20, CD56, CD57, CD15, or MPO. We confirmed from the raw images that

133 CD3, CD4, and CD8 were not internalized, indicating activation, nor did these cells express other  
134 T cell activation markers CD45RA, CD45RO, PD-1, or LAG-3 (Figure 1.C, Supplemental Figure 1A,  
135 bottom right). This population could represent a type of innate lymphoid cell<sup>34</sup> and was labeled  
136 “Granzyme-B<sup>+</sup>/CD3<sup>-</sup>”.

## 137 **Islet- and extra-islet regions are altered in T1D**

138 We first sought to identify cellular changes in T1D within islets specifically. Previous reports  
139 observed that insulin-containing islets are significantly more common in recent-onset T1D cases  
140 than cases with diabetes durations of greater than one year<sup>27,35,36</sup>. Similarly, we found that  
141 samples from patients who had been diagnosed with T1D for 0-2 years had significantly reduced  
142  $\beta$ -cell frequencies compared to non-T1D controls. Furthermore, samples from subjects with  
143 disease durations of 5-6 years had minimal remaining  $\beta$ -cell mass (Figure 1.D). Whereas one AA+  
144 case had  $\beta$ -cell mass comparable to those of cases with disease duration of 0-2 years, the other  
145 AA+ case was comparable to non-T1D controls (Figure 1.D). The total islet area imaged was  
146 comparable across all donors (Supplemental Figure 1.B).

147 Next, we investigated how the abundances of non-endocrine cell types inside islets differed  
148 across donors. We performed Principal Component Analysis (PCA) on the donors using the  
149 frequencies of non-endocrine cell types located in islets. Donors were clearly separated into two  
150 groups by the first two principal components; one group included all T1D cases and one AA+ case  
151 and the second included all non-T1D cases and the other AA+ case (Figure 1.E). In this analysis,  
152 we did not consider  $\beta$ -cells,  $\alpha$ -cells, and  $\delta$ -cells. Thus, donors were stratified by disease duration  
153 strictly according to the abundances of immune and other pancreatic, non-endocrine cell types  
154 in the islets.

155 We next considered only cells located outside islets. Again, donors were clearly separable by the  
156 first two principal components (Figure 1.F). The first principal component separated cases with  
157 times since diagnosis between 0-2 years from non-T1D, AA+, and cases with diabetes durations  
158 of 5-6 years (Figure 1.F). The second principal component separated cases with diabetes  
159 durations of 5-6 years from the rest (Figure 1.F). Therefore, both the islet and extra-islet spaces  
160 of T1D and non-T1D cases were distinct.

161 Many cell types were increased in T1D cases with times since diagnosis of 0-2 years relative to  
162 non-T1D controls (Supplemental Figure 1C). In T1D cases with times since diagnosis of 5-6 years,  
163 the abundance of different cell types either remained higher than non-T1D controls or returned  
164 to baseline (Supplemental Figure 1.C). This trend was present in both islet and extra-islet regions.  
165 These data demonstrate that the immune activity between the islet and extra-islet  
166 compartments are coordinated.

## 167 **Pseudotemporal reconstruction of islet pathogenesis** 168 **identifies a conserved trajectory of insulinitis**

169 In human T1D,  $\beta$ -cell destruction does not occur simultaneously across all islets and even  
170 neighboring islets can be at different stages of destruction<sup>18,26,27</sup>. We therefore used pseudotime

171 analysis to infer the most likely progression of a single islet through disease space<sup>18</sup>. To develop  
172 a pseudotemporal map, we quantified the cellular composition of each islet, including cells within  
173 20  $\mu\text{m}$  of the islet's boundary, and applied the pseudotime algorithm PArTition-based Graph  
174 Abstraction (PAGA)<sup>37</sup> (Figure 2.A; Figure 2.B). PAGA was selected because it is a high-performing  
175 algorithm able to identify multiple trajectories, if they exist, while making minimal assumptions  
176 about the true structure<sup>38</sup>.

177 Displayed in Figure 2.B is the PAGA force-directed layout where each point represents an islet.  
178 Each islet's color reflects the pseudotemporal distance from the centroid of non-T1D islets. As  
179 expected, the islets from different donor groups (no T1D, AA+, T1D) had different distributions  
180 across the PAGA map (Figure 2.C ). In the PAGA map, a continuum is apparent from islets  
181 abundant in insulin-expressing  $\beta$ -cells on the left of the map to islets depleted in  $\beta$ -cells on the  
182 right (Figure 2.D, Figure 2.E, Figure 2.F, top row). PAGA uses Leiden clustering internally, enabling  
183 the following regions of the pseudotime map to be labelled objectively: 1) Islets with low  
184 pseudotime values on the left of the map (PAGA-internal Leiden clusters 0 and 5 in Supplemental  
185 Figure 2.A) were labelled "Normal" even if they originated from T1D donors. 2) Islets in the  
186 middle of the map (PAGA-internal Leiden clusters 6, 2, and 8 in Supplemental Figure 2.A) were  
187 elevated in HLA-ABC (MHC Class I) expression, CD8<sup>+</sup>T cells, and macrophage/DCs (Figure 2.D,  
188 Figure 2.E, Figure 2.F, rows 2-4) and were labelled "Inflamed". 3) Islets with late pseudotime  
189 values on the right of the map (PAGA-internal Leiden clusters 1, 3, 7, and 4 in Supplemental Figure  
190 2.A) were devoid of  $\beta$ -cells and were labelled "Insulin-Depleted" (Figure 2.D, Figure 2.E, Figure  
191 2.F, top row).

192 In addition, islets lacking  $\beta$ -cells occasionally contained CD8<sup>+</sup>T cells and were labelled "Insulin-  
193 Depleted + Immune Islets" (Figure 2.D, Figure 2.E, Figure 2.F, rows 2-4). The presence of these  
194 islets suggests that signals retaining CD8<sup>+</sup>T cells in islets linger after  $\beta$ -cells die. The distribution  
195 of all cell types across pseudotime is reported in Supplemental Figure 2.B.

196 Islets from non-T1D controls and one of the AA+ donors (6314) were primarily in the Normal  
197 group to the left of the map (Figure 2.C , Supplemental Figure 2.C). Islets from subjects who had  
198 had T1D for of 5-6 years (cases 6195 and 6323) were primarily in the Insulin-Depleted group to  
199 the right of the map (Figure 2.C , Supplemental Figure 2.C). Islets from the remaining T1D donors  
200 and the other AA+ donor were distributed broadly throughout the map (Figure 2.C ,  
201 Supplemental Figure 2.C).

202 We quantified the fraction of each cell type in swaths at varying distances from the islet edge.  
203 We found that for B Cells, CD4<sup>+</sup>T cells, CD8<sup>+</sup>T cells, macrophage/DCs, neutrophils, and plasma  
204 cells, the fraction of the given cell type in the islet relative to outside the islets increased  
205 (Supplemental Figure 2.D), demonstrating that the inflammation in islets was distinct from the  
206 inflammation in the extra-islet tissue. Thus, immune cells were targeting islets specifically.

207 Together, these results illustrate a single, non-branching progression from Normal Islets to  
208 Insulin-Depleted Islets via Inflamed Islets, consistent with previous pseudotime analyses<sup>18</sup>.

## 209 **IDO expression on islet vasculature is linked to T cell** 210 **infiltration**

211 We observed islets with vasculature staining positive for indoleamine 2, 3-dioxygenase 1 (IDO).  
212 In the tumor microenvironment, IDO is commonly expressed by myeloid cells and suppresses  
213 CD8<sup>+</sup>T cell activity through multiple mechanisms, including the induction of FOXP3<sup>+</sup> regulatory T  
214 cells and the inhibition of CD8<sup>+</sup>T cell function<sup>39</sup>. In islets, IDO co-stained with CD31<sup>+</sup> vasculature  
215 but not CD45<sup>+</sup> immune cells adjacent to vasculature (Figure 2.G). IDO was not expressed by  
216 endocrine or other cell types in islets or by vasculature or any cell type outside islets  
217 (Supplemental Figure 2.E). We manually quantified vascular expression of IDO on islets  
218 throughout pseudotime and found that all but two IDO<sup>+</sup> islets were in the Inflamed group (Figure  
219 2.H). Therefore, IDO expression by islet vasculature was tightly associated with insulinitis.

220 A potent inducer of IDO expression is Interferon- $\gamma$  (IFN- $\gamma$ ), a cytokine highly expressed by  
221 activated T cells and macrophages<sup>39</sup>. Therefore, we hypothesized that IDO expression was  
222 induced by infiltrating immune cells during insulinitis. We compared the frequency of CD8<sup>+</sup>T cells  
223 and macrophage/DCs in islets from the Inflamed group with and without IDO<sup>+</sup> vasculature and  
224 found that CD8<sup>+</sup>T cells were significantly more abundant in islets with IDO<sup>+</sup> vasculature than islets  
225 without IDO<sup>+</sup> vasculature (Figure 2.I). In addition, the expression of HLA-ABC, another interferon-  
226 stimulated gene, was higher in  $\beta$ -cells in IDO<sup>+</sup> islets than in  $\beta$ -cells in IDO<sup>-</sup> islets (Supplemental  
227 Figure 2.F). However, the abundance of  $\gamma\delta$ -T cells and CD4<sup>+</sup>T cells was less strongly associated  
228 with IDO<sup>+</sup> vasculature and the abundance of macrophage/DCs was not significantly associated  
229 with IDO<sup>+</sup> vasculature (Supplemental Figure 2.F).

230 In summary, IDO expression by islet vasculature is positively associated with T cell infiltration and  
231 may be an immunoregulatory checkpoint.

## 232 **Insulinitis has sub-states, defined by functional states of** 233 **CD8<sup>+</sup>T cells**

234 CD8<sup>+</sup>T cells are a major component of insulinitis (row 4 of Figure 2.E and Figure 2.F) and are capable  
235 of directly and indirectly killing  $\beta$ -cells. A comprehensive description of the activation profiles of  
236 CD8<sup>+</sup>T cells could provide insight into their roles in T1D pathogenesis. To obtain extremely high-  
237 quality marker quantification, we trained a neural network on manually labelled images of single  
238 T cells (Figure 3.A, Supplemental Figure 3.A). Using our neural network, we quantified the  
239 expression of T cell markers on islet CD8<sup>+</sup>T cells (Figure 3.B).

240 PD-1, TOX, CD45RO, CD69, and CD44—markers of antigen experience—were the markers most  
241 frequently expressed by islet-infiltrating CD8<sup>+</sup>T cells (Figure 3.B, Supplemental Figure 3.B). CD8<sup>+</sup>T  
242 cells expressing CD45RA (which are either naïve or terminally differentiated effector memory  
243 cells (TEMRA)) were detectable in islets, as previously reported<sup>18</sup> (Figure 3.B). In addition, we  
244 observed a rare population of CD45RO<sup>+</sup> CD8<sup>+</sup>T cells co-expressing Lag-3, Granzyme-B, and ICOS  
245 (Figure 3.B bottom clade). Lastly, a rare population of CD57<sup>+</sup> CD8<sup>+</sup>T cells was present but these  
246 cells rarely co-expressed LAG-3, Granzyme-B, or ICOS (Figure 3.B top clade). These populations

247 resemble the two exhausted T cell populations identified in the peripheral blood of T1D patients  
248 that were associated with responsiveness to alefacept<sup>40</sup>. Therefore, the activation profiles of  
249 islet-infiltrating T cells are heterogeneous.

250 We reasoned that the islet microenvironment may dictate the activation state of CD8<sup>+</sup>T cells by  
251 specifically recruiting T cells of a particular state or inducing changes after they enter the islet. If  
252 so, islets would contain specific combinations of CD8<sup>+</sup>T cell states. To interrogate this, we  
253 performed UMAP only on Inflamed islets, using the frequencies of CD8<sup>+</sup>T cells expressing each  
254 functional marker. We identified four inflamed sub-clusters, I-IV, (Figure 3.C top). Here, the term  
255 “sub-cluster” is used to highlight that these groups were all contained within the previously  
256 defined “Inflamed” cluster and the roman numerals do not imply a temporal ordering. Inflamed-  
257 I contained only CD8<sup>+</sup>T cells that did not express any of the functional markers analyzed (Figure  
258 3.C bottom, top row). Inflamed-II was characterized by a high frequency of CD45RA<sup>+</sup>CD8<sup>+</sup>T cells  
259 (Figure 3.C bottom, second row from top and Figure 3.D top row). Inflamed-III was characterized  
260 by a low frequency of CD45RA<sup>+</sup> cells and high frequency of CD45RO<sup>+</sup> and PD-1<sup>+</sup> cells (Figure 3.C  
261 bottom, third row from top and Figure 3.D middle row). Inflamed-IV was characterized by an  
262 enrichment of CD8<sup>+</sup>T cells expressing CD57, LAG-3, ICOS, Granzyme-B, PD-1 or CD45RO (Figure  
263 3.C bottom, bottom row and Figure 3.D bottom row). In summary, the phenotypes of CD8<sup>+</sup>T cells  
264 are coordinated across islets.

## 265 **Regulation of insulitis sub-states by the islet** 266 **microenvironment**

267 To identify cellular or molecular factors that regulate the state of CD8<sup>+</sup>T cells in islets, we first  
268 inspected the distribution of inflamed sub-clusters in each patient. Each donor possessed islets  
269 that belonged to multiple inflamed islet sub-clusters (Figure 3.E). Therefore donor-level factors  
270 such as genetics, the location within the pancreas (i.e. head, body, or tail), or time since T1D  
271 onset, are not associated. Instead, these insulitis sub-states are conserved among T1D patients.

272 Next, we asked if each T cell marker is enriched in CD8<sup>+</sup>T cells in islets compared to CD8<sup>+</sup>T cells in  
273 the peri-islet and exocrine space. We computed the frequencies of each CD8<sup>+</sup>T cell state inside  
274 islets of each inflamed sub-cluster and in separate swaths 0-25 $\mu$ m, 25-50 $\mu$ m and 50-100 $\mu$ m away  
275 from the islets (Supplemental Figure 3.C). We found that for islets of Inflamed-II, -III, and -IV,  
276 functional markers characterizing their CD8<sup>+</sup>T cells were expressed more frequently inside than  
277 in the surrounding tissue areas. Although the different functional markers were all enriched on  
278 islet-infiltrating T cells compared to T cells outside islets, the degree of this enrichment varied  
279 across the markers measured (Supplemental Figure 3.C). The markers of Inflamed-IV, LAG-3,  
280 ICOS, and Granzyme-B, were highly enriched inside islets (~20% of islet-infiltrating CD8<sup>+</sup>T cells vs  
281 <5% of extra-islet CD8<sup>+</sup>T cells). CD45RA and CD69 in Inflamed-II were slightly less enriched in  
282 islets (~28% of islet-infiltrating and ~20% of extra-islet CD8<sup>+</sup>T cells). CD45RO and PD-1 in  
283 Inflamed-III islets were the most abundant but had the least enrichment in islets (~45% of islet-  
284 infiltrating CD8<sup>+</sup>T cells vs ~35% of extra-islet CD8<sup>+</sup>T cells) (Supplemental Figure 3.C). This  
285 demonstrated that the specific differences in the compositions of CD8<sup>+</sup>T cell states in different  
286 islets were attributable to the islet microenvironment and not the surrounding extra-islet spaces.



287 Although macrophage/DCs are abundant in islets from the Inflamed group (Figure 2.E, Figure  
288 2.F) and can interact with T cells by presenting antigen or secreting cytokines, neither the  
289 expression of markers of macrophage/DC activity nor macrophage/DC abundance was  
290 significantly associated with any of the inflamed sub-clusters (Supplemental Figure 3.D). Similarly,  
291 no other cell-type nor the vascular expression of IDO was linked to CD8<sup>+</sup>T cell programs in islets  
292 (Supplemental Figure 3.D). Accordingly, the four inflamed sub-clusters had identical distributions  
293 throughout the original PAGA force-directed layout (Figure 3.F). Therefore, the activation states  
294 of islet-infiltrating T cells are independent of the abundance of any of the other cell types we  
295 could identify.

296 Lastly, we compared CD8<sup>+</sup>T cells in islets from the Insulin-Depleted + Immune group to CD8<sup>+</sup>T  
297 cells in islets from the Inflamed group. Insulin-Depleted + Immune islets contained a higher  
298 frequency of CD45RA<sup>+</sup> CD8<sup>+</sup>T cells and a lower frequency of CD45RO<sup>+</sup> CD8<sup>+</sup>T cells than Inflamed  
299 islets (Figure 3.G). TOX was expressed by a higher frequency of CD8<sup>+</sup>T cells in Insulin-Depleted +  
300 Immune islets than CD8<sup>+</sup>T cells in Inflamed islets (Figure 3.G). Importantly, CD45RA<sup>+</sup> and TOX  
301 were never co-expressed on the same CD8<sup>+</sup>T cell (Figure 3.B). These data indicate that the  
302 activation state or persistence of these two populations in islets depends on insulin expression.

## 303 **Vasculature, nerves, and Granzyme-B<sup>+</sup>/CD3- cells** 304 **outside islets are associated with lobular patterning**

305 In the pancreas, islets are grouped within lobules. In some donors, the destruction of islets in T1D  
306 exhibits a strong lobular patterning: that is, insulin-positive, immune-infiltrated, and insulin-  
307 negative islets are each primarily found in different lobules<sup>41</sup>. However, other donors are on the  
308 other end of this spectrum and have lobules comprised of a random mixture of islets from  
309 different stages of pathogenesis.

310 It is unknown why some cases exhibit lobular patterning. One explanation could be an islet-  
311 intrinsic mechanism where the expression of programs sensitizing beta cells to immune-killing  
312 (i.e. stress) are correlated across islets in the same lobule. Alternatively, it could be mediated by  
313 cells outside islets if they facilitate extravasation into the lobule or trafficking from one afflicted  
314 islet to the next.

315 To systematically investigate lobular patterning in T1D, we used a neural network to segment  
316 lobules and assign each single cell and islet to its lobule. We first quantified the degree of lobular  
317 patterning within each donor using the intra-class correlation coefficient (ICC). The ICC ranges  
318 from 0 to 1 where cases with values closer to 1 have islets whose states are more synchronized  
319 within lobules (Figure 4.A). Islets of non-T1D cases and 6314, 6195, and 6323 did not have  
320 appreciable variability in their pseudotimes, but in the remaining cases, the ICCs ranged from  
321 0.17 to 0.74 (Figure 4.B). This highlights that the magnitude of lobular patterning ranges widely  
322 across T1D cases with insulinitis.

323 We employed hierarchical linear modeling (HLM), a statistical framework designed to identify  
324 relationships between levels of multi-level data. HLMs are standard in fields where multi-level  
325 data are common such as Education, in which students are grouped into classrooms, which are  
326 grouped into schools (Gelman et al. 2014) and have been applied in biomedical settings<sup>43,44</sup>. We

327 were interested in cell-types if their abundance in a lobule correlated with the lobule's average  
328 islet pseudotime. Importantly, we omitted the islet region itself from the calculation of a cell  
329 type's lobular abundance because we were interested in identifying features in the extra-islet  
330 space that were associated with islet destruction. For each cell type, we estimated the effect of  
331 its total abundance in a lobule (the number of cells divided by the number of acinar cells to  
332 normalize for lobule area) on the pseudotimes of islets in that lobule. We performed this analysis  
333 in two-level HLMs for each donor and a three-level HLM considering all donors together (Figure  
334 4.C).

335 We identified three cell types — vasculature, nerves, and Granzyme-B<sup>+</sup>/CD3<sup>-</sup> cells — that were  
336 significantly associated with lobules across multiple T1D tissue donors. All three were more  
337 abundant in lobules with islets late in pseudotime (Figure 4.C boxed rows, Figure 4.D). Samples  
338 from cases 6323 and 6195 which had very few insulin-containing islets had increased abundances  
339 of vasculature, Granzyme-B/CD3<sup>-</sup> cells, and nerves in their extra-islet spaces compared to non-  
340 T1D controls (Supplemental Figure 1C), indicating these changes persist through the point when  
341 the entire tissue is afflicted. In addition, vasculature, Granzyme-B<sup>+</sup>/CD3<sup>-</sup> cells, and nerves were  
342 increased in Inflamed islets compared to Normal islets indicating that they may serve a role in  
343 islets in addition to their role in the extra-islet compartment (Supplemental Figure 4A). Note that  
344 Supplemental Figure 4A differs from Supplemental Figure 1C because islets are broken up  
345 according to pseudotime, not donor, and not all islets in T1D donors are undergoing insulinitis.

346 Counterintuitively, although CD8<sup>+</sup>T cells and macrophage/DCs were higher in the extra-islet  
347 compartments of T1D cases vs non-T1D cases (Supplemental Figure 1C), they were not associated  
348 with lobular patterning (they were not more abundant in the extra-islet space of lobules with  
349 more advanced insulinitis) (Figure 4.C). These data raise the possibility that vasculature, Granzyme-  
350 B/CD3<sup>-</sup> cells, and nerves outside islets help predispose lobules to insulinitis or are affected by  
351 extensive insulinitis.

## 352 **Immature tertiary lymphoid structures are enriched in** 353 **subjects with T1D**

354 We hypothesized that T cells' interactions with certain cell types in specific areas of the pancreas  
355 may be important for their functionality. Therefore, we identified Cellular Neighborhoods  
356 (CNs)<sup>30,45</sup>, tissue regions that are homogeneous and have defined cell-type compositions. To  
357 identify CNs, single cells were clustered according to the cell-type composition of their twenty  
358 nearest spatial neighbors and automatically annotated with the names of enriched cell types  
359 (Figure 5.A, See Methods). This resulted in 75 CNs. Throughout the manuscript, CNs are referred  
360 to with the nomenclature (Cell Type A|Cell Type B|...) to indicate all the cell types that are  
361 enriched in them (See Methods).

362 Next, we identified CNs that were more abundant in T1D than non-T1D tissues (Figure 5.B). The  
363 top three CNs (fold change of abundance in T1D relative to abundance in non-T1D) were (CD8<sup>+</sup>T  
364 cells|B Cells), (Macrophage|Stromal Cells|B Cells), and (Vasculature|B Cells) (Figure 5.B, Figure  
365 5.C). We asked whether these three CNs were commonly adjacent to each other as this could  
366 indicate that they act as components of a larger structure<sup>45</sup>. Measuring the frequency with which

367 the three B cell CNs were adjacent to each other throughout the tissues demonstrated that the  
368 (CD8<sup>+</sup>T cells|B Cells) CN is predominantly found adjacent to both the other CNs but that  
369 (Macrophage|Stroma|B Cells) and (Vasculature|B Cells) are less commonly adjacent to each  
370 other (Figure 5.D).

371 We next asked whether these CN assemblies corresponded to either peri-vascular cuffs<sup>46,47</sup> or  
372 tertiary lymphoid structures (TLSs)<sup>17,46,48</sup>, as these are two B Cell-rich structures commonly  
373 present in autoimmune conditions. Although the (CD8<sup>+</sup>T cells|B Cells) CN was adjacent to vessels  
374 (Figure 5.D, Figure 5.E), it was not in the perivascular space, as is the case with perivascular cuffs  
375 (Figure 5.E). In our samples, the (CD8<sup>+</sup>T cells|B Cells) CN did not have segregated T cell and B cell  
376 zones as seen in mature TLSs, consistent with<sup>17</sup>.

377 In summary, the (CD8<sup>+</sup>T cells|B Cells) CN is more abundant in T1D tissues from patients with  
378 diabetes durations of 0-2 years compared to non-T1D tissues and T1D tissue from patients who  
379 had T1D for more than 4 years.

## 380 **Immature tertiary lymphoid structures are in the extra-** 381 **islet pancreas, and are enriched in CD45RA<sup>+</sup> /CD8<sup>+</sup> T cells**

382 We next asked whether the (CD8<sup>+</sup>T cells|B Cells) CN had high endothelial venules (HEV),  
383 specialized blood vessels that are commonly found in TLSs that enable naïve lymphocytes to  
384 extravasate into peripheral tissues. We observed expression of peripheral lymph node addressin  
385 (PNA<sup>+</sup>), an HEV marker, in the vessels associated with the (CD8<sup>+</sup>T cells|B Cells) CN (Figure 5.E left  
386 image) but not in other vessels (data not shown). Although we could not assess the presence of  
387 other TLS traits such as follicular dendritic cells, fibroblastic reticular cells, or follicular helper T  
388 cells, the aggregation of B cells and presence of HEVs, but the lack of compartmentalized B and  
389 T cell zones indicate that instances of the (CD8<sup>+</sup>T cells|B Cells) CN are immature TLSs.

390 Next, we asked if immature TLSs could support the entry of naïve CD8<sup>+</sup>T cells into the pancreas.  
391 We observed CD8<sup>+</sup>T cells co-expressing CD45RA and CD62L (the ligand for PNA<sup>+</sup>) near PNA<sup>+</sup>  
392 vasculature (Figure 5.E, middle and right image respectively). Thus, CD45RA<sup>+</sup>/CD8<sup>+</sup>T cells in the  
393 pancreas can adhere to HEVs. Furthermore, CD45RA<sup>+</sup> was enriched three-fold on CD8<sup>+</sup>T cells in  
394 the (CD8<sup>+</sup>T cells|B Cells) CN relative to CD8<sup>+</sup>T cells in the tissue as a whole (Figure 5.F), providing  
395 additional evidence that CD45RA<sup>+</sup> T cells may enter the pancreas through HEVs.

396 We found immature TLS both adjacent (Figure 5.G.1) or not adjacent (Figure 5.G.2) to islets.  
397 Quantifying the frequency of this adjacency revealed that fewer than half of the immature TLS  
398 were adjacent to islets (Figure 5.H). We did not identify any differences in the cellular  
399 composition of the immature TLS that were or were not adjacent to islets (Supplemental Figure  
400 5A). We reasoned that even if immature TLSs were far from islets, extravasating cells may migrate  
401 to islets. Accordingly, islet-adjacent CD45RA<sup>+</sup> CD8<sup>+</sup>T cells (that were not in islet-adjacent TLSs) co-  
402 expressed CD62L, suggesting that they originated from the (CD8<sup>+</sup>T cells|B Cell) CN (Figure 5.I).  
403 Consistent with this, in one notable tissue donor, regions of the pancreas with Insulin-Depleted  
404 islets were enriched in the (CD8<sup>+</sup>T cells|B Cell) CN relative to regions of the pancreas with β-cell  
405 containing islets (Figure 5.J). This spatial correlation between the (CD8<sup>+</sup>T cells|B Cells) CN and

406 the destruction of islets implicates immature TLS with islet pathology even if they are not  
407 adjacent to islets (Figure 5.J).

## 408 Discussion

409 We have performed CODEX imaging and comprehensive computational analysis of whole  
410 cadaveric pancreata from T1D subjects. Our data support several conclusions.

411 First, our results are consistent with the model previously proposed by Damond et al, who  
412 proposed a single trajectory for insulinitis, characterized by an enrichment in HLA-ABC expression,  
413 CD8<sup>+</sup>T cells, and macrophage/DCs<sup>18</sup>.

414 Second, we are the first to report that IDO<sup>+</sup> vasculature is present in inflamed islets but not in  
415 normal islets or islets that have lost insulin-expression (Figure 2.G, Figure 2.H). Furthermore,  
416 islets with IDO<sup>+</sup> vasculature contained higher frequencies of CD8<sup>+</sup>T cells and higher expression of  
417 HLA-ABC, but not higher frequencies of macrophage/DCs compared to inflamed islets that did  
418 not contain IDO<sup>+</sup> vasculature, suggesting that IDO is induced by a cytokine produced by  
419 infiltrating CD8<sup>+</sup>T cells such as IFN- $\gamma$  (Figure 2.I). Given IDO's established tolerogenic role, these  
420 data suggest that the loss of IDO on vasculature could be a prerequisite for  $\beta$ -cell death.  
421 Leveraging this checkpoint to protect transplanted  $\beta$ -cells from rejection has shown promise<sup>49</sup>  
422 and could be combined with similar approaches using programmed death-ligand 1<sup>50,51</sup>

423 We did not observe IDO expression on  $\beta$ -cells, in contrast to Anquetil et al. that report this in  
424 healthy patients<sup>52</sup>. Our observations are consistent with data demonstrating that IDO needs to  
425 be induced. First, it has been shown with western blot and RT-PCR that human islets require  
426 cytokine stimulation to express IDO<sup>53</sup>. Second, the human protein atlas has tested multiple IDO  
427 antibodies and demonstrated that IDO is negative in human islets via immunohistochemistry:  
428 (<https://www.proteinatlas.org>). In addition, the human protein atlas's single-cell RNAseq atlas  
429 only report IDO transcripts in immune cells in healthy pancreas.

430 Third, we performed the first high-dimensional spatial phenotyping of CD8<sup>+</sup>T cells in T1D islets.  
431 We found that most T cells were antigen experienced. A small population expressed CD45RA and  
432 CD69, which could be naïve, TEMRA, or Tscm cells (Figure 3.B). Another population expressed  
433 Lag-3, Granzyme-B, and ICOS. It is notable that only a small population of islets had Granzyme-B-  
434 expressing T cells. This could indicate that alternative mechanisms are contributing to the  
435 elimination of  $\beta$ -cells.

436 Fourth, the insulinitis trajectory is comprised of four sub-clusters, each characterized by the  
437 activation profile of the islet-infiltrating CD8<sup>+</sup>T cells (Figure 3.C). Multiple of these inflamed sub-  
438 clusters were present in all T1D donors. One potential explanation for this observation is that  
439 sub-clusters are capable of inter-converting (Figure 3.E). The factors that regulate the conversion  
440 of a given islet between sub-clusters could correspond to immunoregulatory checkpoints that  
441 are critical to the progression of T1D. Unfortunately, our search for such features failed to  
442 generate any candidates (Supplemental Figure 3.D). By phenotyping T cells at different distances  
443 from the islet edge, we were able to determine that the T cell activation profiles characterizing  
444 each sub-cluster were only present in the islet, not in the surrounding tissue (Supplemental  
445 Figure 3.C). Unfortunately, from our data, we cannot speculate whether the insulinitis sub-clusters

446 arose due to differential stimulation of T cells that had already entered islets, differential  
447 recruitment of pre-activated T cells, or both.

448 Fifth, pancreatic lobules affected by insulinitis are characterized by distinct tissue markers. We  
449 discovered that lobules enriched in  $\beta$ -cell-depleted islets were also enriched in nerves,  
450 vasculature, and Granzyme-B<sup>+</sup>/CD3<sup>-</sup> cells, suggesting these factors may make lobules permissive  
451 to disease (Figure 4.C). The role of islet innervation in T1D has been studied but such work has  
452 focused on nerves in the islet rather than on nerves in the exocrine tissue<sup>54</sup>. The Granzyme-  
453 B<sup>+</sup>/CD3<sup>-</sup> cells could be natural killer cells; if so, they are most likely of the CD56dim subset as  
454 CD56 was not detected on these cells. It is noteworthy that the cell types linked with direct islet  
455 invasion were distinct from those linked to lobule patterning even though both sets of cell types  
456 were found across islet and extra-islet regions. Therefore, for insulinitis to consume every islet,  
457 crosstalk may be required between the cell types in the islet and extra-islet compartments.  
458 Conversely, inhibiting this interaction might contain pathology to isolated lesions.

459 Finally, we identify immature TLS away from islets where CD45RA<sup>+</sup> CD8<sup>+</sup>T cells aggregate. We  
460 also observed an inflamed islet-subcluster characterized by an abundance of CD45RA<sup>+</sup>/CD8<sup>+</sup> T  
461 cells. It will be important to determine whether the CD45RA<sup>+</sup> T cells localized around islets may  
462 have originated from immature TLS. In mice, blocking immune egress from lymph nodes reduced  
463 the size of TLSs and halted diabetes<sup>55</sup>. Thus, therapeutic targeting of immune cell trafficking to  
464 TLS could help mitigate autoimmunity in human T1D.

465 Together, these data illuminate relationships between insulinitis, the local islet microenvironment  
466 and inflammation at distal sites.

467 A major limitation for the study is the cohort size. Cases with documented insulinitis are very rare,  
468 significantly limiting the feasibility of curating large cohorts<sup>35</sup>. Due to this limitation, factors such  
469 as the donors' histories of drug use, durations of stay in the intensive care unit, and BMIs could  
470 not be balanced or statistically adjusted for but should be considered as they may affect exocrine  
471 inflammation but not the prevalence of insulinitis<sup>29,56</sup>. In addition, only one of the AA+ cases, Case  
472 6267, had detectable insulinitis (Figure 2.C). The other case, 6314 tested positive for only one  
473 autoantibody, GADA+, and therefore had a significantly lower probability of progressing to overt  
474 T1D<sup>57</sup>. Age and diabetes duration are also important criteria to consider when interpreting key  
475 results (Supplemental Figure 5B-C).

476 Another limitation is our limited perspective on myeloid cell populations. Although antibodies in  
477 our panel detect numerous myeloid markers, we failed to identify any heterogeneity in myeloid  
478 populations during insulinitis. This was likely due in part to the difficulty of segmenting myeloid  
479 cells and quantifying marker expression due to their morphology. Spatial transcriptomics could  
480 be used in future studies to better define the myeloid populations and inform additions to future  
481 CODEX panels.

482 Lastly, our samples are 2-dimensional sections which could affect some of the adjacency  
483 relations.

484 In conclusion, using a data-driven approach, we mapped conserved sub-states of insulinitis and  
485 integrated the spatial pathology of islet and extra-islet regions into a single model of T1D  
486 pathogenesis. The tools and computational pipelines developed here will enable further

487 investigation of immune pathology at the tissue scale that may lead to development of therapies  
488 for T1D.  
489

## 490 **Methods**

### 491 **Human tissues**

492 Cadaveric pancreatic FFPE tissue sections were obtained through the nPOD program, sponsored  
493 by the Juvenile Diabetes Research Fund. Case numbers cited herein are assigned by nPOD and  
494 comparable across nPOD-supported projects. 17 cases in the nPOD biorepository had been  
495 previously documented to contain insulinitis. For each of these 17 cases, we examined the triple  
496 stained immunohistochemistry images (CD3, Insulin, and Glucagon) using nPOD's online  
497 pathology database to select blocks in which insulinitis was present. To ensure that the tissue  
498 regions still contained insulinitis (and had not been sectioned extensively after their images were  
499 uploaded to the nPOD pathology database), we re-sectioned and visualized CD3, Insulin, and  
500 Glucagon. The use of cadaveric human tissue samples is approved by Stanford University's  
501 Institutional Review Board.  
502

### 503 **CODEX data collection**

504 *CODEX Antibody Generation and Validation.* Oligonucleotides were conjugated to purified,  
505 carrier-free, commercially available antibodies as previously described<sup>30,58</sup>. For validation  
506 experiments, human tonsils and non-diabetic pancreata were co-embedded in FFPE blocks so  
507 both tissues could be stained and imaged simultaneously. Each antibody in the CODEX panel was  
508 validated by co-staining with previously established antibodies targeting positive and negative  
509 control cell types. Once validated, the concentration and imaging exposure time of each antibody  
510 were optimized. The tissue staining patterning was compared to the online database, The Human  
511 Protein Atlas, and the published literature. The specificity, sensitivity, and reproducibility of  
512 CODEX staining has been previously validated<sup>30,31,58-60</sup>  
513

514 *CODEX Staining.* Staining and imaging was conducted as previously described<sup>30,58-60</sup>. Briefly, FFPE  
515 tissues were deparaffinized and rehydrated. Heat-induced epitope retrieval (HIER) antigen  
516 retrieval was conducted in Tris/EDTA buffer at pH9 (Dako) at 97°C for 10 minutes. Tissues were  
517 blocked for 1 hour with rat and mouse Ig, salmon-sperm DNA, and a mixture of the non-  
518 fluorescent DNA oligo sequences used as CODEX barcodes. Tissues were stained with the  
519 antibody cocktail in a sealed humidity chamber overnight at 4°C with shaking. The next day,  
520 tissues were washed, fixed with 1.6% paraformaldehyde, 100% methanol, and BS3 (Thermo  
521 Fisher Scientific), and mounted to a custom-made acrylic plate attached to the microscope.  
522

523 *CODEX Imaging.* Imaging was conducted using the Keyence BZ-X710 fluorescence microscope  
524 with a CFI Plan Apo  $\lambda$  20x/0.75 objective (Nikon). "High resolution" mode was selected in Keyence  
525 Navigator software, resulting in a final resolution of .37744  $\mu\text{m}/\text{pixel}$ . The exposure times are  
526 listed in Supplemental Table 3. Regions for imaging were selected by rendering HLA-ABC,  
527 Proinsulin, and CD8 and selecting large regions (averaging 55mm<sup>2</sup>). The full antibody panel and

528 cycle-ordering is detailed in (Supplemental Tables 3 and 4). Biotinylated hyaluronan-binding  
529 protein was rendered by adding streptavidin-PE at 1:500 concentration to the 96 well plate  
530 containing fluorescent oligos in the last cycle and running the CODEX program normally. DRAQ5  
531 was added to the last cycle because we found it stained nuclei more evenly than HOECHST which  
532 slightly improved segmentation. Each tissue took between 3 and 7 days to image depending on  
533 the tissue area.

534  
535 *Characterization of Tertiary Lymphoid Structures.* A serial section from case 6228 was imaged in  
536 a separate CODEX experiment using an antibody panel tailored for characterizing tertiary  
537 lymphoid structures, as described in Supplemental Table 3. These data were acquired and  
538 analyzed identically to the main dataset.

539  
540 *Image Pre-processing.* Drift compensation, deconvolution, z-plane selection was performed using  
541 the CODEX Toolkit uploader ([github.com/nolanlab/CODEX](https://github.com/nolanlab/CODEX)). Cell segmentation using the DRAQ5  
542 nuclear channel and lateral bleed compensation was performed with CellSeg<sup>33</sup>.

543  
544 **Cell Type Clustering and Annotation**  
545 Marker expression was z-normalized within each donor and subsequently clustered in two steps.  
546 First, cells were projected into 2 dimensions using the markers indicated in Supplemental Table  
547 2 and Parametric Uniform Manifold Approximation and Projection (pUMAP)<sup>62</sup> was applied on a  
548 downsampled dataset. The fit model was used to transform the remaining cells. Cell types were  
549 gated using Leiden clustering and manual merging. The cluster containing immune cells was sub-  
550 clustered using the markers detailed in Supplemental Table 2. Acinar cells contaminating the  
551 Immune cluster were gated out and merged with the Acinar cluster from the previous step. The  
552 Endocrine class was sub-clustered into  $\alpha$ -,  $\beta$ -, and  $\delta$ -Cells using Glucagon, Proinsulin, and  
553 Somatostatin respectively. Clusters were annotated according the heatmap marker expression,  
554 and overlaying annotations onto raw images (Supplemental Figure 1.A) using custom scripts in  
555 Fiji.

556  
557 **Islet Segmentation and Pseudotime**  
558 *Preprocessing.* Windows consisting of the twenty nearest spatial neighbors surrounding each  
559 single cell were clustered according to their cell-type composition using Mini Batch K Means with  
560  $k=200$ . For this analysis,  $\alpha$ -,  $\beta$ -, and  $\delta$ -Cells were combined into one 'Endocrine' cell type. One  
561 cluster was highly enriched in Endocrine cells and accurately defined the islet area. Individual  
562 islets were identified using the connected components algorithm and filtering out islets that had  
563 fewer than ten total cells.

564  
565 *PAGA Analysis.* For each islet, the number of each cell type inside the islet and between the islet  
566 edge and 20 $\mu$ m beyond were extracted. To adjust for variation due to the islet size, the cell type  
567 counts were divided by the number of endocrine cells inside the islet. Data were then log-  
568 transformed. The PAGA embedding was computed using the default parameters except for the  
569 following: The neighborhood search was performed using cosine distance and 15 nearest  
570 neighbors; Leiden clustering used a resolution of 1. For computing the pseudotime values (used

571 in the colormap in Figure 2B, the x-axis in Figure 2F, and Figure 4), the path through the inflamed  
572 islet was isolated by temporarily omitting 25 islets positioned in the middle of the map between  
573 Normal and Insulin-Depleted islets. Only 9 of these were from T1D or AA+ donors.  
574

## 575 Quantification and Validation of Functional Marker Gating

576 *Annotation of Ground-Truth Dataset.* 4000 CD8<sup>+</sup>T cells were labelled for fifteen markers by an  
577 immunologist familiar with the staining patterns of each marker using VGG Image annotator<sup>63</sup>.  
578

579 *Automated Thresholding.* For each functional marker of interest, the lateral-bleed-compensated  
580 mean fluorescence<sup>33</sup> of cell types known to not express the marker in question were used to  
581 calculate a background distribution. Marker-positive cells were defined as those whose  
582 expression was greater than the 99<sup>th</sup> percentile of the background distribution.  
583

584 *Gating with Neural Network:* 22 $\mu$ m x 22 $\mu$ m cropped images of each single cell were used as  
585 training data. The marker that the image corresponded to was not included as an input in the  
586 neural network and one classifier was trained for all markers. Cells were split into training,  
587 validation, and test splits (60/15/25 respectively). ResNet50 architecture and initial weights were  
588 imported from the Keras library pre trained on ImageNet. Image augmentation consisted of  
589 random flips, rotations, zooms, contrast, and translation (+/- ten pixels only). All weights were  
590 unfrozen, and the model was trained for 100 epochs (see accompanying source code for training  
591 details).  
592

## 593 Sub-clustering of Inflamed Islets with Cell-Type specific Functional 594 Markers

595 For each Inflamed Islet (n=351), the frequency of each marker expressed by CD8<sup>+</sup>T cells was  
596 computed. Single cells inside the islet and within 20 $\mu$ m from the islet's edge were combined  
597 before the frequency was measured. The subsequent matrix underwent z-normalization  
598 followed by UMAP gating using Bokeh. Insulin-Depleted + Immune Islets were defined as islets  
599 without  $\beta$ -cells with greater than two CD8<sup>+</sup>T cells and greater than seven macrophage/DCs. These  
600 thresholds correspond to the 95<sup>th</sup> percentiles of CD8<sup>+</sup>T cells and macrophage/DCs in Normal  
601 islets.  
602

## 603 Identification of Cellular Neighborhoods

604 Previously, CNs<sup>30</sup> were identified by, for each single cell, defining its 'window' as the 20 spatial  
605 nearest neighbors. Cells were clustered according to the number of each cell type in their  
606 windows using Mini Batch K-Means. The output clusters corresponded to CNs. To ensure our  
607 method was sensitive to rare neighborhoods, we adapted this algorithm by intentionally over-  
608 clustering, using k=200 in the K- Means step rather than using a k ranging from 10-20 as used  
609 elsewhere<sup>31,45,64</sup>. Next, to determine which cell types were characteristic of each cluster, we  
610 identified, for each cluster, the set of cell-types that were present in more than 80% of the  
611 windows allocated to that cluster. We named the clusters according to this set of cell-types and  
612 merged all clusters with the same name, resulting in seventy-five CNs. Acinar cells and epithelial



613 cells were used in the kNN graph and in the clustering but were not considered when merging  
614 clusters. Note that this method does not differentiate neighborhoods that have the same  
615 combination of cell types but different stoichiometries.

## 616 Lobule Segmentation

617 A training dataset was generated by manually tracing the edges of lobules in ImageJ using the  
618 ROI function. The ROI were then floodfilled in Python and used as masks for training. For each  
619 tile, the blank cycle was selected to distinguish tissue from background coverslip. A U-Net  
620 model was trained for 10 epochs (see attached source code for training details). After stitching  
621 together all masks, the resulting images required slight refinement where lobules were not  
622 completely separated, and this was done manually in ImageJ. The connected components in the  
623 stitched image defined the lobule instances. Cells were assigned to a lobule by indexing the  
624 lobule mask with their X and Y coordinates. Cells in the inter-lobular space were assigned to  
625 one “edge” lobule. This resulted in 464 lobules.

626

## 627 Formulation of Hierarchical Linear Models

628 For each lobule, the number of each cell type in the extra-islet space was divided by the  
629 number of acinar cells in the extra-islet space. For all HLMs, the *lme4* package for R was used<sup>65</sup>  
630 and statistical significance was computed using the *lmerTest* package for R<sup>66</sup>. Lobular cell-type  
631 abundance was z-normalized within each donor and the pseudotime was z-normalized across  
632 the entire dataset prior to fitting.

633

634 The ICC was computed using the model:  $pseudotime_{islet} \sim 1|lobuleID$  with the *performance*  
635 package in R. A value of 0 indicates that the variation in pseudotimes of islets within the same  
636 lobule is equal to the variation across all islets in the donor and a value of 1 indicates that the  
637 variation in pseudotimes of islets within the same lobule is much smaller than that of all islets in  
638 the donor.

639

640 For each cell type, a two-level, random intercept HLM within each donor was constructed with  
641 the following formulation (in R formula syntax):  $pseudotime_{islet} \sim celltype_{lobule} + (1|lobuleID)$  and  
642 a three-level random intercept, random slope HLM including islets from all donors was  
643 formulated:  $pseudotime_{islet} \sim celltype_{lobule} + (1 + celltype_{lobule} | donorID) + (1|lobuleID)$ . Here,  
644  $pseudotime_{islet}$  equals the pseudotime of each islet,  $celltype_{lobule}$  equals the number of the given  
645 cell type in a particular lobule divided by the number of acinar cells in that lobule, z-normalized  
646 within each donor, and  $lobuleID$  and  $donorID$  are categorical variables specifying the lobule and  
647 donor that the given islet belongs to.

648

## 649 Neighborhood Adjacency

650 The adjacency between neighborhoods was computed as in<sup>45</sup>. The only modification was that  
651 neighborhood instances were identified using connected components of the k-NN graph with k=5  
652 rather than from the thresholded images.

## 653 **Data Availability**

654 Processed single cell dataframes are accessible at:

655

656 <https://www.dropbox.com/sh/8sqef3iwjb6f4wp/AAAQzFgDOgMBiWh9Jqcb81U8a?dl=0>.

657

658 The raw and stitched, processed data is hosted by the BioImage Archive

659 (<https://www.ebi.ac.uk/bioimage-archive/>) with the accession number

660 S-BIAD859.

## 661 **Code Availability**

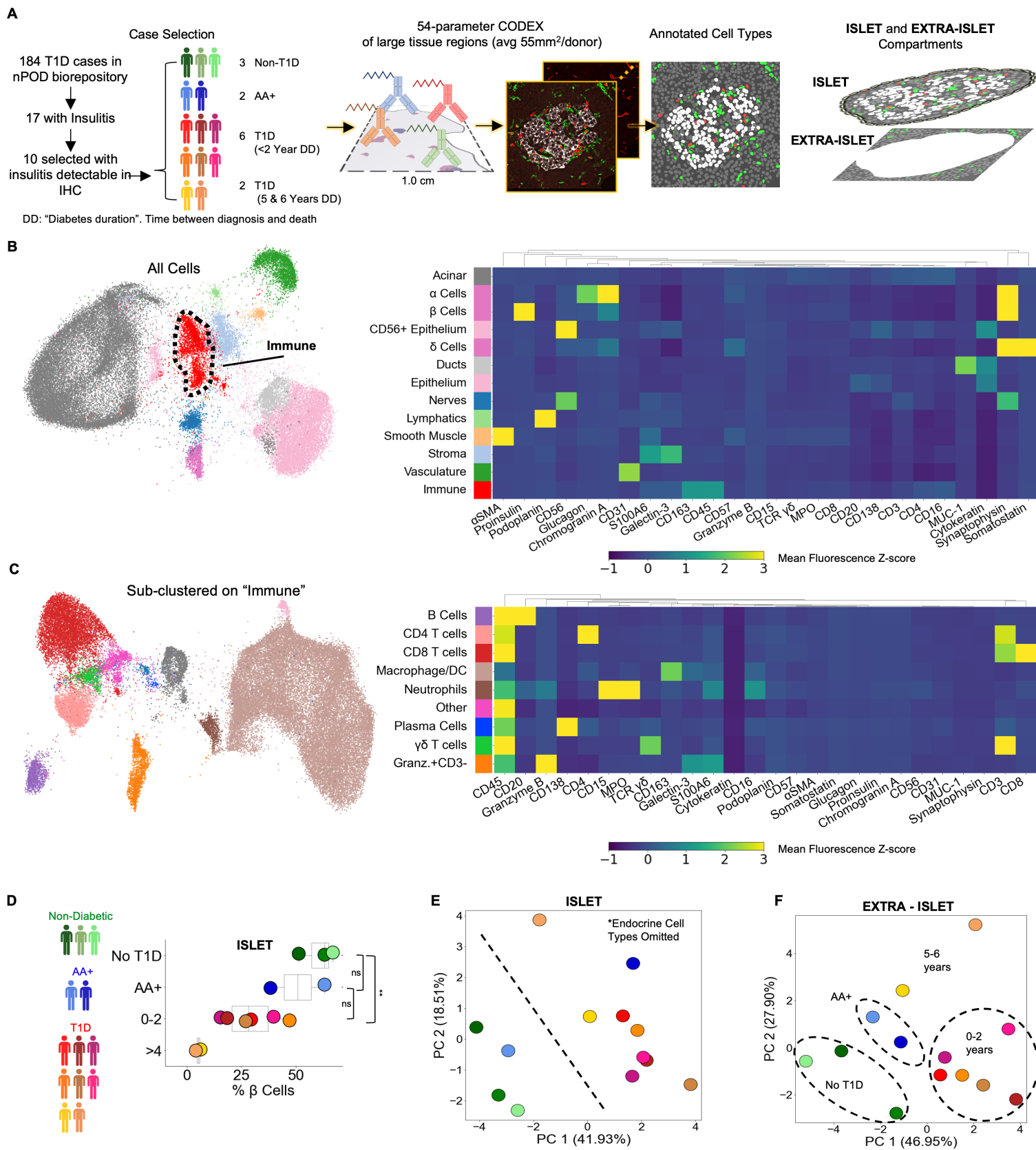
662 All primary code is attached with the supplementary information and will be posted on the Nolan

663 Lab's github upon acceptance. The code is completely open source. The code is not intended as

664 a software tool and so no small example data set is applicable.

665

666



667 **Figure 1 Profiling T1D pancreata with CODEX high-parameter imaging reveals alterations**  
668 **in the cellular composition of islet and extra-islet compartments.**

669 Figure 1.A Left: Schematic of the workflow for selection of nPOD cases. Blues, greens, and reds  
670 indicate non-T1D, AA+, or T1D status, respectively. Center: Schematic for acquisition and  
671 processing of CODEX highly multiplexed imaging dataset. Right: Schematic of islet and extra-islet  
672 pancreatic regions.

673 Figure 1.B UMAP and Leiden clustering of major cell types. Colors match those in the heatmap  
674 shown to the right. Heatmap of mean z-normalized marker expression in each cell-type cluster.  
675 Only a subset of the markers used for the UMAP are included in the heatmap to facilitate  
676 visualization. A full description of the markers used for the clustering stages is available in  
677 Supplemental Table 2.

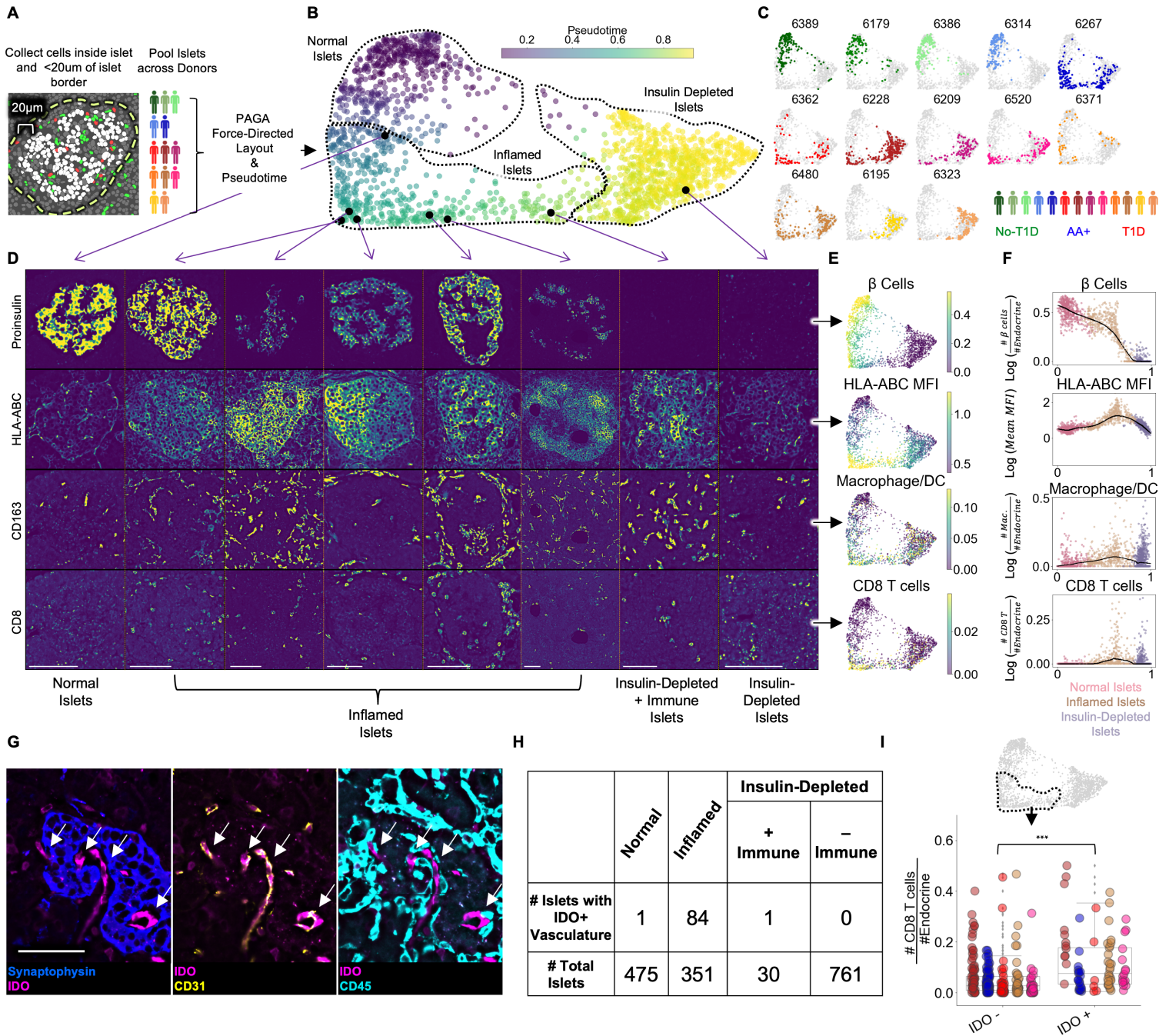
678 Figure 1.C UMAP of the immune population identified in Figure 1B further clustered using  
679 additional immune markers as described in Supplemental Table 2. Colors match those in heatmap  
680 shown in the heatmap to the right. The heatmap is generated in an identical manner as the  
681 heatmap in Figure 1B.

682 Figure 1.D Frequency of  $\beta$ -Cells per donor determined by dividing the number of  $\beta$ -cells by the  
683 total number of  $\beta$ -cells,  $\alpha$ -cells, and  $\delta$ -Cells. Blues, greens, and reds indicate non-T1D, AA+, or  
684 T1D status, respectively. Significance was determined using the t-test (\*  $p < 0.05$ , \*\*  $p < 0.01$ , \*\*\*  
685  $p < 0.001$ )

686 Figure 1.E Principal component analysis of the islet compartment. The number of cells of each  
687 cell type (omitting  $\alpha$ -,  $\beta$ -, and  $\delta$ -cells) were divided by the number of endocrine cells to adjust for  
688 different islet areas. Blues, greens, and reds indicate non-T1D, AA+, or T1D status, respectively.

689 Figure 1.F Principal component analysis of the extra-islet compartment. The number of cells of  
690 each cell type (omitting  $\alpha$ -,  $\beta$ -, and  $\delta$ -cells) were divided by the number of acinar cells to adjust  
691 for different areas imaged. Blues, greens, and reds indicate non-T1D, AA+, or T1D status,  
692 respectively.

693



694 **Figure 2 Pseudotemporal reconstruction of insulinitis identifies IDO on islet vasculature.**

695 Figure 2.A Schematic of islet segmentation and quantification of islet cellular composition.

696 Figure 2.B PAGA-force directed layout of islets colored by pseudotime. The start point of  
697 pseudotime was calculated as the centroid of the non-T1D islets. Representative islets from  
698 different stages of pseudotime are indicated with black points and their raw images are depicted  
699 in Figure 2.D. Normal, Inflamed, and Insulin-Depleted groups were obtained by merging the  
700 clusters output by the PAGA algorithm (Supplemental Figure 2.A).

701 Figure 2.C Islet distribution across pseudotime for each donor. The titles indicate nPOD case IDs  
702 as in Supplemental Table 1. The frequency of islets from each donor in each stage of islet  
703 pseudotime is reported in Supplemental Figure 2.C.

704 Figure 2.D Images of Proinsulin, HLA-ABC, CD163, and CD8 staining in islets representative of  
705 different points along pseudotime as indicated in B. Scale bars (lower left of each column)  
706 indicate 100 $\mu$ m.

707 Figure 2.E Quantification of selected features across pseudotime overlaid onto the PAGA force-  
708 directed layout. For  $\beta$ -cells, macrophage/DCs, and CD8<sup>+</sup>T cells, the values correspond to log(#  
709 cells/# endocrine cells). For HLA-ABC, the mean HLA-ABC expression for each cell in the islet was  
710 computed and log transformed.

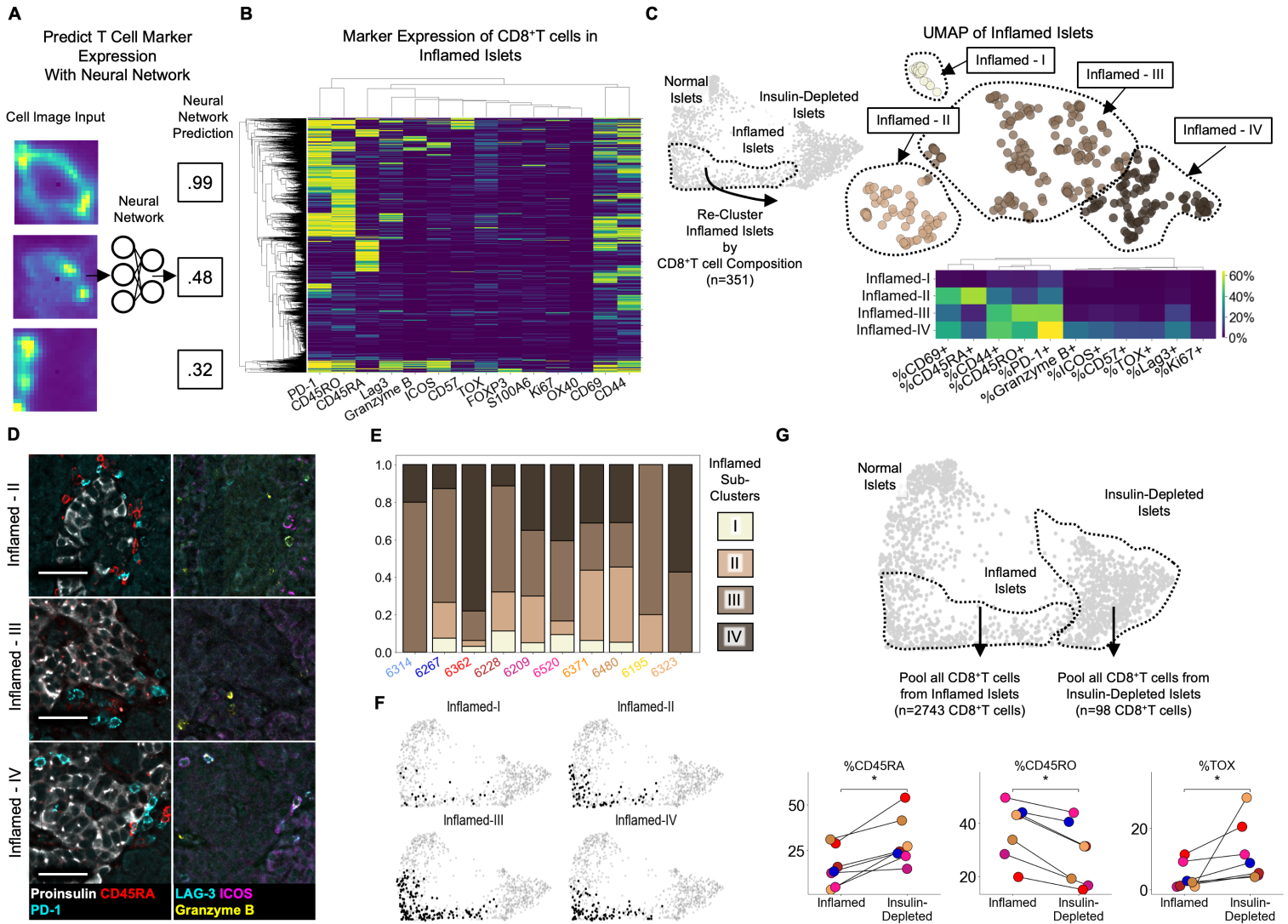
711 Figure 2.F Quantification of selected features across pseudotime. For  $\beta$ -cells, macrophage/DCs,  
712 and CD8<sup>+</sup>T cells, the values correspond to log(# cells/# endocrine cells). For HLA-ABC, the mean  
713 HLA-ABC expression for each cell in the islet was computed and log transformed. Color legend:  
714 Normal islets: pink; Inflamed islets: brown; Insulin-Depleted islets: purple. Black points  
715 demarcate LOWESS regression.

716 Figure 2.G Representative image of an islet from the Inflamed group stained with IDO and, from  
717 left to right, Synaptophysin, CD31, and CD45. Arrows indicate IDO<sup>+</sup>/CD31<sup>+</sup> vasculature. Right  
718 shows that IDO<sup>+</sup> cells are negative for CD45 and therefore, are not immune cells associated with  
719 vasculature. Scale bar (bottom left image) indicates 50  $\mu$ m.

720 Figure 2.H Distribution of IDO expression on islet vasculature across pseudotime.

721 Figure 2.I Association of IDO<sup>+</sup> islet vasculature with islet CD8<sup>+</sup>T cell density. The y-axis corresponds  
722 to the number of CD8<sup>+</sup>T cells per endocrine cell per islet. CD8<sup>+</sup>T cell counts were normalized to  
723 adjust for islet size. The x-axis indicates whether islets contain IDO<sup>+</sup> vasculature. Each color  
724 corresponds to a donor. All donors with detectable IDO<sup>+</sup> islet vasculature are displayed: 6480,  
725 6267, 6520, 6228, and 6362. Colors are same as in Figure 2.C. IDO<sup>+</sup> vasculature was manually  
726 quantified. For combined donors, significance was determined with a mixed-effect linear model,  
727  $p = 1.5 \times 10^{-12}$  (Satterthwaites's method lmerTest R package). The complete breakdown per  
728 donor is reported in Supplemental Figure 2.F.

729



730 **Figure 3 Insulitis has sub-states, characterized by CD8<sup>+</sup>T cell functionality**

731 Figure 3.A Schematic of marker-quantification with a ResNet50 neural network. Raw images are  
732 input, and the neural network outputs a number between 0 and 1 indicative of the level of  
733 confidence that the cell expresses that marker with 1 indicating the highest confidence.

734 Figure 3.B Heatmap of all 2,855 Inflamed Islet CD8<sup>+</sup>T cells, hierarchically clustered according to  
735 marker expression predicted by the neural network.

736 Figure 3.C Top) UMAP of Inflamed Islets based on frequencies of markers on CD8<sup>+</sup>T cells in islets.  
737 Bottom) Mean frequencies of each marker on CD8<sup>+</sup>T cells in islets of each inflamed sub-cluster.

738 Figure 3.D Representative images of islets from each subcluster with associated immune markers.  
739 Scale bars indicate 50  $\mu$ m.

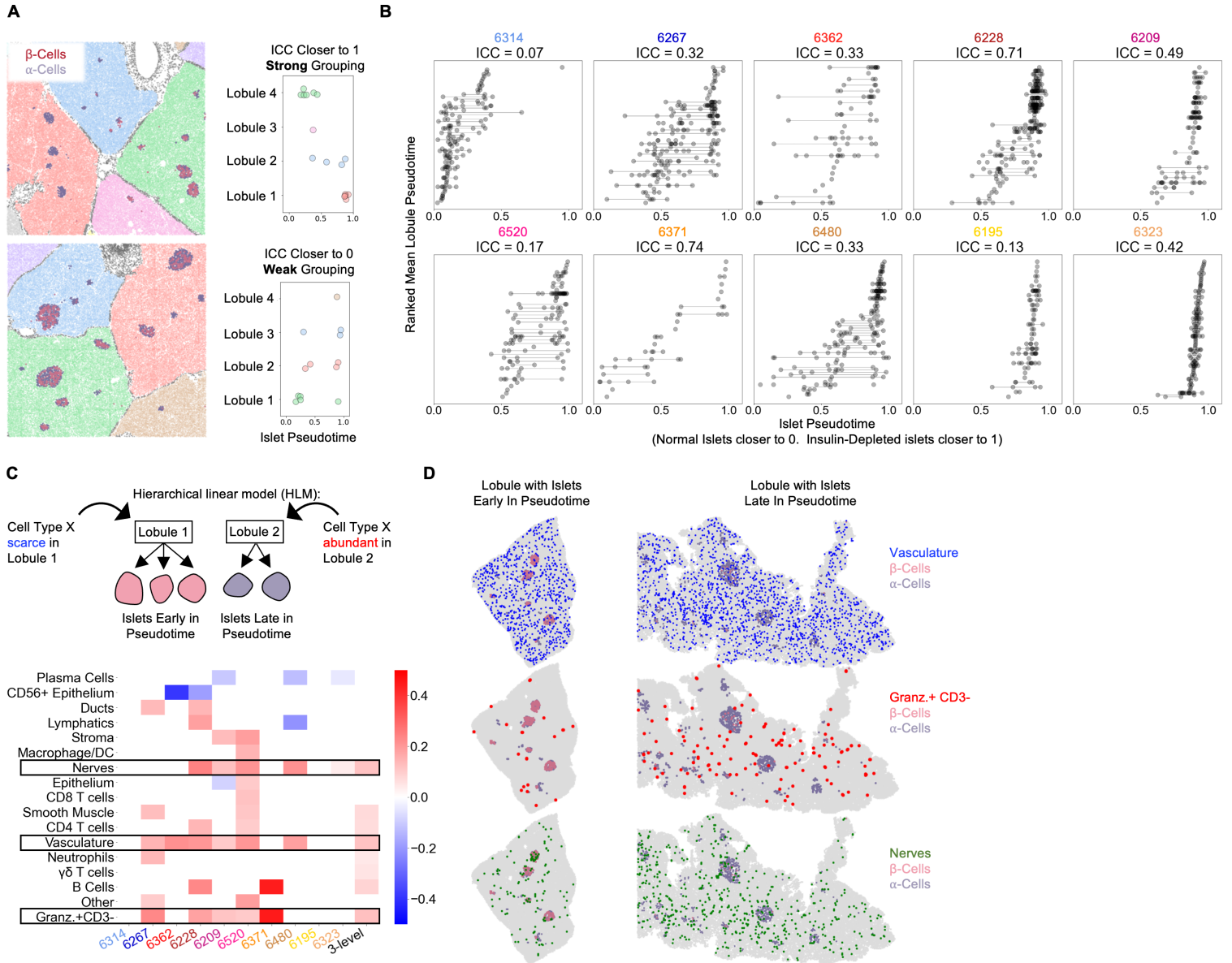
740 Figure 3.E Frequencies of islets from each subcluster per donor in AA+ and T1D samples. Color  
741 indicates subcluster as in panel C.

742 Figure 3.F Distribution of the islets of Inflamed-I through -IV on the PAGA force-directed layout  
743 shown in Figure 2.B

744 Figure 3.G Differences in marker expression frequencies between CD8<sup>+</sup>T cells in islets from the  
745 Inflamed group and from the Insulin-Depleted + Immune group. T cells from all islets of the  
746 specified groups were pooled within each donor to compute the frequencies of marker  
747 expression. Significance was determined using the Wilcoxon signed-rank test (\*  $p < 0.05$ , \*\*  
748  $p < 0.01$ , \*\*\*  $p < 0.001$ ) and was not corrected for multiple hypothesis testing.

749





750 **Figure 4 Vasculature, nerves, and Granzyme-B<sup>+</sup>/CD3<sup>-</sup> cells in the extra-islet pancreas are**  
751 **associated with the lobular patterning of islet pathogenesis**

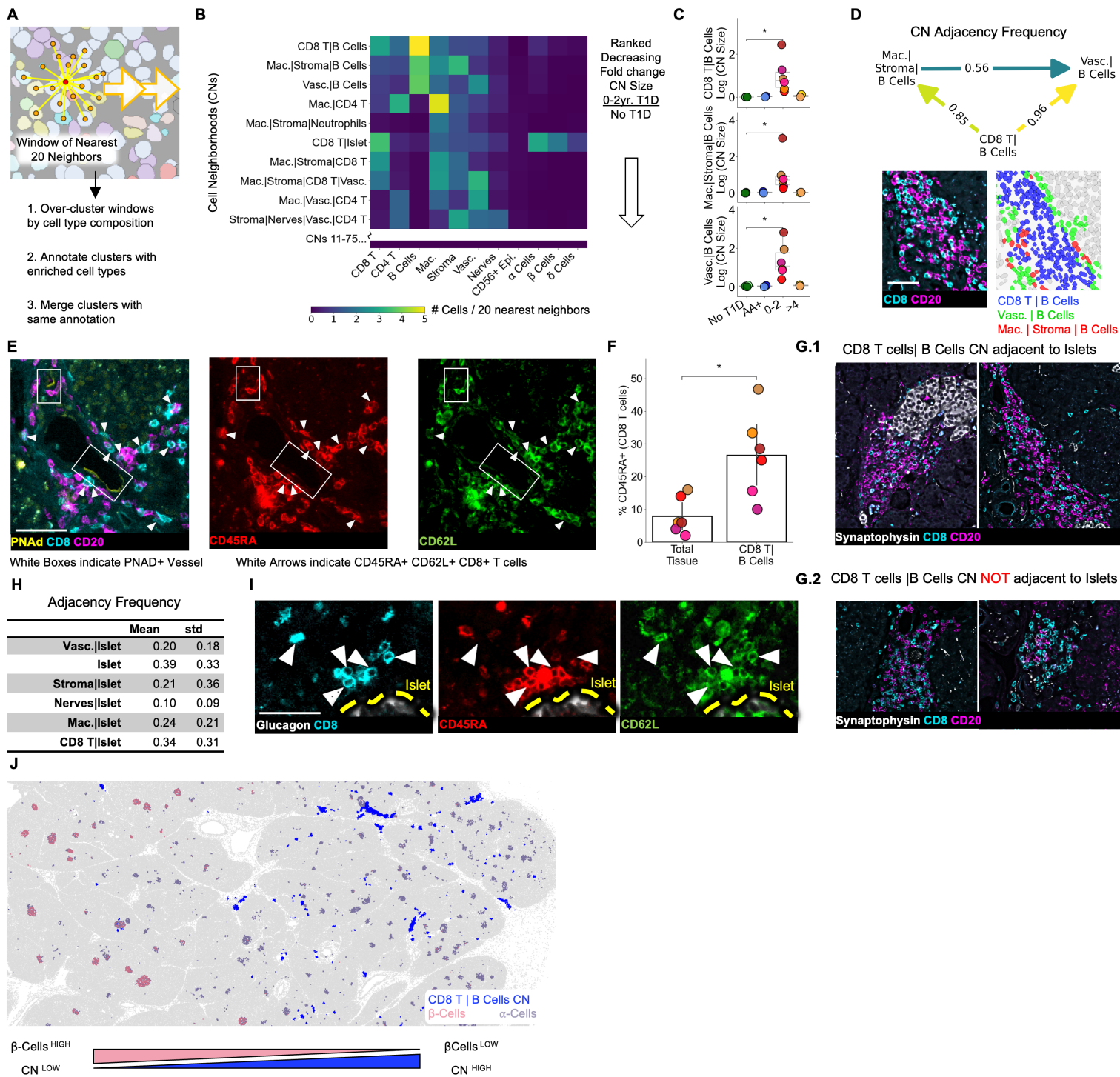
752 Figure 4.A A schematic of the method for quantifying lobular patterning of insulinitis. Lobules were  
753 segmented and colored accordingly. The islets are colored according to their composition of b-  
754 cells and a-cells. Top: A region from case 6228 with a strong lobular grouping effect and an ICC  
755 closer to 1. Bottom: A region from case 6267 with a weak lobular grouping effect and an ICC  
756 closer to 0.

757 Figure 4.B Lobular patterning of insulinitis within each donor. Each point represents an islet. The x-  
758 axis represents the islet pseudotime. The y-axis is ordinal, representing the rank of each lobule  
759 according to the mean pseudotime of its islets. Violin plots per lobule are overlaid. Abbreviations:  
760 ICC: Intraclass correlation coefficient.

761 Figure 4.C Cell types associated with lobular patterning. Top: Schematic of the hierarchical linear  
762 model. Cells in islets were omitted when computing the lobular abundance of each cell-type.  
763 Bottom: Coefficients of two-level models trained on each donor separately (columns labeled by  
764 donor) and a three-level model (right column). Color corresponds to the coefficient and features  
765 with  $p > 0.05$  are white. Significance was determined using Satterthwaites's method in the  
766 lmerTest R package. No adjustment for multiple hypothesis testing was applied.

767 Figure 4.D Visualization of vasculature (top), Granzyme-B/CD3<sup>-</sup> cells (middle), and nerves  
768 (bottom) in two lobules. The left lobule represents lobules with islets earlier in pseudotime and  
769 a lower abundance of the given cell type in the lobule. The right lobule represents lobules with  
770 islets late in pseudotime and a greater abundance of the given cell type in the lobule.

771



772 **Figure 5 Immature tertiary lymphoid structures far from islets are potential staging areas for**  
773 **islet-destined CD8<sup>+</sup>T cells**

774 Figure 5.A Schematic of algorithm for identifying CNs. Red point indicates index cell for the CN.  
775 Orange points indicate the nearest neighbors of the index cell. Windows are collected for each  
776 cell in the dataset (indicated by orange arrows).

777 Figure 5.B Cell-type compositions of the top CNs organized in decreasing order of the fold  
778 increase in abundance in T1D vs. non-T1D samples. Each column in the heatmap indicates the  
779 mean density of that cell type in the 20 nearest spatial neighbors of cells assigned to the CN  
780 designated for that row. CN abundance was calculated as the number of cells assigned to the  
781 given CN divided by the number of acinar cells. Abbreviations: Vasc.: vasculature; Mac.:  
782 macrophage/DCs; Lym.: lymphatics. Neu.: neutrophils; CD8 T: CD8<sup>+</sup>T cells; CD4 T: CD4<sup>+</sup>T cells.  
783 Endocrine cell types were merged during CN annotation and are labeled “Islet”.

784 Figure 5.C Mean abundances of the CD8<sup>+</sup>T cell and B cell CNs per donor. Abundance was  
785 calculated as the number of cells assigned to the given CN divided by the number of acinar cells.  
786 Significance was determined using the Mann-Whitney U test (\* p<0.05, \*\* p<0.01, \*\*\* p<0.001).  
787 No adjustment for multiple hypothesis testing was applied.

788 Figure 5.D Top: Adjacency frequencies of (CD8<sup>+</sup>T cells | B Cell CN) with (Macrophage | Stroma | B  
789 Cells) and (Vasculature | B Cells) CNs. The adjacency frequency was calculated as the number of  
790 instances of the source CN adjacent to the destination CN divided by the total number of  
791 instances of the source CN. Bottom Left: Raw image of a representative assembly of the three  
792 CNs (CD8<sup>+</sup>T cells | B Cell CN), (Macrophage | Stroma | B Cells), and (Vasculature | B Cells) displaying  
793 CD8 and CD20 staining. Bottom Right: The same assembly as to the left colored by CN. Scale bar  
794 indicates 50µm).

795 Figure 5.E Representative images of co-localization of PNA<sup>+</sup> endothelium and CD45RA<sup>+</sup> CD62L<sup>+</sup>  
796 CD8<sup>+</sup>T cells located in the (CD8<sup>+</sup>T cells | B Cells) CN. Scale bar indicates 50µm.

797 Figure 5.F Frequency of CD45RA expression on CD8<sup>+</sup>T cells located in (CD8<sup>+</sup>T cell | B cell) CN  
798 relative to CD8<sup>+</sup>T cells throughout the tissue. Significance was determined with a Wilcoxon  
799 signed-rank test (\* p<0.05, \*\* p<0.01, \*\*\* p<0.001).

800 Figure 5.G Representative images of (CD8<sup>+</sup>T cells | B Cells) instances adjacent to islets (G.1) and  
801 not adjacent to islets (G.2). Scale bars indicate 200µm.

802 Figure 5.H Quantification of the adjacency frequencies between the (CD8<sup>+</sup>T cells | B Cells) CN and  
803 CNs rich in endocrine cells (i.e “Islet CNs”). Mean, std: mean and standard deviation adjacency  
804 frequency across T1D donors. Abbreviations: Vasc.: vasculature; Mac.: macrophage.

805 Figure 5.I Representative images of islet-adjacent CD45RA<sup>+</sup> CD62L<sup>+</sup> CD8<sup>+</sup>T cells. Scale bar  
806 indicates 50 µm.

807 Figure 5.J Image showing the spatial distribution of the (CD8<sup>+</sup>T cells | B cells) CN instances relative  
808 to islets and the enrichment of (CD8<sup>+</sup>T cells | B cells) CN instances in areas of the pancreas with  
809 islets lacking β-Cells.

## 810 References

- 811 1. Gregory, G. A. *et al.* Global incidence, prevalence, and mortality of type 1 diabetes in 2021  
812 with projection to 2040: a modelling study. *Lancet Diabetes Endocrinol.* **10**, 741–760  
813 (2022).
- 814 2. Hirsch, J. S. FDA approves teplizumab: a milestone in type 1 diabetes. *Lancet Diabetes*  
815 *Endocrinol.* **11**, 18 (2023).
- 816 3. Herold, K. C. *et al.* Teplizumab (Anti-CD3 mAb) Treatment Preserves C-Peptide Responses  
817 in Patients With New-Onset Type 1 Diabetes in a Randomized Controlled Trial: Metabolic  
818 and Immunologic Features at Baseline Identify a Subgroup of Responders. *Diabetes* **62**,  
819 3766–3774 (2013).
- 820 4. Perdigoto, A. L. *et al.* Treatment of type 1 diabetes with teplizumab: clinical and  
821 immunological follow-up after 7 years from diagnosis. *Diabetologia* **62**, 655–664 (2019).
- 822 5. Herold, K. C. *et al.* An Anti-CD3 Antibody, Teplizumab, in Relatives at Risk for Type 1  
823 Diabetes. *N. Engl. J. Med.* **381**, 603–613 (2019).
- 824 6. Pescovitz, M. D. *et al.* Rituximab, B-Lymphocyte Depletion, and Preservation of Beta-Cell  
825 Function. *N. Engl. J. Med.* **361**, 2143–2152 (2009).
- 826 7. Orban, T. *et al.* Co-stimulation modulation with abatacept in patients with recent-onset type  
827 1 diabetes: a randomised, double-blind, placebo-controlled trial. *Lancet Lond. Engl.* **378**,  
828 412–419 (2011).
- 829 8. Orban, T. *et al.* Costimulation Modulation With Abatacept in Patients With Recent-Onset  
830 Type 1 Diabetes: Follow-up 1 Year After Cessation of Treatment. *Diabetes Care* **37**, 1069–  
831 1075 (2014).
- 832 9. Bluestone, J. A., Buckner, J. H. & Herold, K. C. Immunotherapy: Building a bridge to a cure  
833 for type 1 diabetes. *Science* **373**, 510–516 (2021).
- 834 10. Krogvold, L. *et al.* Pancreatic biopsy by minimal tail resection in live adult patients at the  
835 onset of type 1 diabetes: experiences from the DiViD study. *Diabetologia* **57**, 841–843  
836 (2014).
- 837 11. Campbell-Thompson, M. *et al.* Network for Pancreatic Organ Donors with Diabetes (nPOD):  
838 Developing a Tissue Biobank for Type 1 Diabetes. *Diabetes Metab. Res. Rev.* **28**, 608–617  
839 (2012).
- 840 12. Pugliese, A. *et al.* The Juvenile Diabetes Research Foundation Network for Pancreatic Organ  
841 Donors with Diabetes (nPOD) Program: goals, operational model and emerging findings.  
842 *Pediatr. Diabetes* **15**, 1–9 (2014).
- 843 13. Wilcox, N. S., Rui, J., Hebrok, M. & Herold, K. C. Life and death of  $\beta$  cells in Type 1  
844 diabetes: a comprehensive review. *J. Autoimmun.* **71**, 51–58 (2016).
- 845 14. Arif, S. *et al.* Blood and Islet Phenotypes Indicate Immunological Heterogeneity in Type 1  
846 Diabetes. *Diabetes* **63**, 3835–3845 (2014).
- 847 15. Leete, P. *et al.* Differential Insulinitic Profiles Determine the Extent of  $\beta$ -Cell Destruction and  
848 the Age at Onset of Type 1 Diabetes. *Diabetes* **65**, 1362–1369 (2016).
- 849 16. Martino, L. *et al.* Mast cells infiltrate pancreatic islets in human type 1 diabetes.  
850 *Diabetologia* **58**, 2554–2562 (2015).
- 851 17. Korpos, É. *et al.* Identification and characterisation of tertiary lymphoid organs in human  
852 type 1 diabetes. *Diabetologia* **64**, 1626–1641 (2021).
- 853 18. Damond, N. *et al.* A Map of Human Type 1 Diabetes Progression by Imaging Mass  
854 Cytometry. *Cell Metab.* **29**, 755-768.e5 (2019).

- 855 19. Wang, Y. J. *et al.* Multiplexed In Situ Imaging Mass Cytometry Analysis of the Human  
856 Endocrine Pancreas and Immune System in Type 1 Diabetes. *Cell Metab.* **29**, 769-783.e4  
857 (2019).
- 858 20. Rodriguez-Calvo, T., Ekwall, O., Amirian, N., Zapardiel-Gonzalo, J. & von Herrath, M. G.  
859 Increased Immune Cell Infiltration of the Exocrine Pancreas: A Possible Contribution to the  
860 Pathogenesis of Type 1 Diabetes. *Diabetes* **63**, 3880–3890 (2014).
- 861 21. Campbell-Thompson, M., Rodriguez-Calvo, T. & Battaglia, M. Abnormalities of the  
862 Exocrine Pancreas in Type 1 Diabetes. *Curr. Diab. Rep.* **15**, 79 (2015).
- 863 22. Bender, C., Rodriguez-Calvo, T., Amirian, N., Coppieters, K. T. & von Herrath, M. G. The  
864 healthy exocrine pancreas contains preproinsulin-specific CD8 T cells that attack islets in  
865 type 1 diabetes. *Sci. Adv.* **6**, eabc5586 (2020).
- 866 23. Fasolino, M. *et al.* Single-cell multi-omics analysis of human pancreatic islets reveals novel  
867 cellular states in type 1 diabetes. *Nat. Metab.* **4**, 284–299 (2022).
- 868 24. Korpos, É. *et al.* The Peri-islet Basement Membrane, a Barrier to Infiltrating Leukocytes in  
869 Type 1 Diabetes in Mouse and Human. *Diabetes* **62**, 531–542 (2013).
- 870 25. Savinov, A. Y., Wong, F. S., Stonebraker, A. C. & Chervonsky, A. V. Presentation of  
871 Antigen by Endothelial Cells and Chemoattraction Are Required for Homing of Insulin-  
872 specific CD8+ T Cells. *J. Exp. Med.* **197**, 643–656 (2003).
- 873 26. In't Veld, P. Insulitis in human type 1 diabetes: a comparison between patients and animal  
874 models. *Semin. Immunopathol.* **36**, 569–579 (2014).
- 875 27. In't Veld, P. Insulitis in human type 1 diabetes: The quest for an elusive lesion. *Islets* **3**, 131–  
876 138 (2011).
- 877 28. Atkinson, M. A. & Mirmira, R. G. The pathogenic “symphony” in type 1 diabetes: A  
878 disorder of the immune system,  $\beta$  cells, and exocrine pancreas. *Cell Metab.* **35**, 1500–1518  
879 (2023).
- 880 29. Bruggeman, B. S. *et al.* Substance Use Affects Type 1 Diabetes Pancreas Pathology:  
881 Implications for Future Studies. *Front. Endocrinol.* **12**, (2021).
- 882 30. Schürch, C. M. *et al.* Coordinated Cellular Neighborhoods Orchestrate Antitumoral  
883 Immunity at the Colorectal Cancer Invasive Front. *Cell* **183**, 838 (2020).
- 884 31. Phillips, D. *et al.* Immune cell topography predicts response to PD-1 blockade in cutaneous T  
885 cell lymphoma. *Nat. Commun.* **12**, 6726 (2021).
- 886 32. Hickey, J. W., Tan, Y., Nolan, G. P. & Goltsev, Y. Strategies for Accurate Cell Type  
887 Identification in CODEX Multiplexed Imaging Data. *Front. Immunol.* **12**, (2021).
- 888 33. Lee, M. Y. *et al.* CellSeg: a robust, pre-trained nucleus segmentation and pixel quantification  
889 software for highly multiplexed fluorescence images. *BMC Bioinformatics* **23**, 46 (2022).
- 890 34. Dalmas, E. *et al.* Interleukin-33-Activated Islet-Resident Innate Lymphoid Cells Promote  
891 Insulin Secretion through Myeloid Cell Retinoic Acid Production. *Immunity* **47**, 928-942.e7  
892 (2017).
- 893 35. Campbell-Thompson, M. *et al.* Insulitis and  $\beta$ -Cell Mass in the Natural History of Type 1  
894 Diabetes. *Diabetes* **65**, 719–731 (2016).
- 895 36. Richardson, S. J. & Pugliese, A. 100 YEARS OF INSULIN: Pancreas pathology in type 1  
896 diabetes: an evolving story. *J. Endocrinol.* **252**, R41–R57 (2022).
- 897 37. Wolf, F. A. *et al.* PAGA: graph abstraction reconciles clustering with trajectory inference  
898 through a topology preserving map of single cells. *Genome Biol.* **20**, 59 (2019).
- 899 38. Saelens, W., Cannoodt, R., Todorov, H. & Saeys, Y. A comparison of single-cell trajectory  
900 inference methods. *Nat. Biotechnol.* **37**, 547–554 (2019).

- 901 39. Munn, D. H. & Mellor, A. L. IDO in the Tumor Microenvironment: Inflammation, Counter-  
902 Regulation, and Tolerance. *Trends Immunol.* **37**, 193–207 (2016).
- 903 40. Diggins, K. E. *et al.* Exhausted-like CD8<sup>+</sup> T cell phenotypes linked to C-peptide preservation  
904 in alefacept-treated T1D subjects. *JCI Insight* **6**, (2021).
- 905 41. Gepts, W. Pathologic Anatomy of the Pancreas in Juvenile Diabetes Mellitus. *Diabetes* **14**,  
906 619–633 (1965).
- 907 42. Gelman, A. *et al.* Bayesian Data Analysis Third edition (with errors fixed as of 15 February  
908 2021). 677.
- 909 43. Jerby-Arnon, L. & Regev, A. DIALOGUE maps multicellular programs in tissue from  
910 single-cell or spatial transcriptomics data. *Nat. Biotechnol.* **40**, 1467–1477 (2022).
- 911 44. Yi, N., Tang, Z., Zhang, X. & Guo, B. BhGLM: Bayesian hierarchical GLMs and survival  
912 models, with applications to genomics and epidemiology. *Bioinformatics* **35**, 1419–1421  
913 (2019).
- 914 45. Bhate, S. S., Barlow, G. L., Schürch, C. M. & Nolan, G. P. Tissue schematics map the  
915 specialization of immune tissue motifs and their appropriation by tumors. *Cell Syst.* (2021)  
916 doi:10.1016/j.cels.2021.09.012.
- 917 46. Agrawal, S. M. *et al.* Extracellular matrix metalloproteinase inducer shows active  
918 perivascular cuffs in multiple sclerosis. *Brain* **136**, 1760–1777 (2013).
- 919 47. Wekerle, H. B cells in multiple sclerosis. *Autoimmunity* **50**, 57–60 (2017).
- 920 48. Rovituso, D. M. *et al.* CEACAM1 mediates B cell aggregation in central nervous system  
921 autoimmunity. *Sci. Rep.* **6**, 29847 (2016).
- 922 49. Alexander, A. M. *et al.* Indoleamine 2,3-Dioxygenase Expression in Transplanted NOD  
923 Islets Prolongs Graft Survival After Adoptive Transfer of Diabetogenic Splenocytes:  
924 *Diabetes* **51**, 356–365 (2002).
- 925 50. Yoshihara, E. *et al.* Immune-evasive human islet-like organoids ameliorate diabetes. *Nature*  
926 **586**, 606–611 (2020).
- 927 51. Castro-Gutierrez, R., Alkanani, A., Mathews, C. E., Michels, A. & Russ, H. A. Protecting  
928 Stem Cell Derived Pancreatic Beta-Like Cells From Diabetogenic T Cell Recognition. *Front.*  
929 *Endocrinol.* **12**, (2021).
- 930 52. Anquetil, F. *et al.* Loss of IDO1 Expression From Human Pancreatic  $\beta$ -Cells Precedes Their  
931 Destruction During the Development of Type 1 Diabetes. *Diabetes* **67**, 1858–1866 (2018).
- 932 53. Sarkar, S. A. *et al.* Induction of indoleamine 2,3-dioxygenase by interferon-gamma in human  
933 islets. *Diabetes* **56**, 72–79 (2007).
- 934 54. Christoffersson, G., Ratliff, S. S. & von Herrath, M. G. Interference with pancreatic  
935 sympathetic signaling halts the onset of diabetes in mice. *Sci. Adv.* **6**, eabb2878 (2020).
- 936 55. Penaranda, C., Tang, Q., Ruddle, N. H. & Bluestone, J. A. Prevention of Diabetes by  
937 FTY720-Mediated Stabilization of Peri-Islet Tertiary Lymphoid Organs. *Diabetes* **59**, 1461–  
938 1468 (2010).
- 939 56. In't Veld, P. *et al.* Beta-cell replication is increased in donor organs from young patients  
940 after prolonged life support. *Diabetes* **59**, 1702–1708 (2010).
- 941 57. Ziegler, A. G. *et al.* Seroconversion to Multiple Islet Autoantibodies and Risk of Progression  
942 to Diabetes in Children. *JAMA* **309**, 2473–2479 (2013).
- 943 58. Kennedy-Darling, J. *et al.* Highly multiplexed tissue imaging using repeated oligonucleotide  
944 exchange reaction. *Eur. J. Immunol.* **51**, 1262–1277 (2021).
- 945 59. Black, S. *et al.* CODEX multiplexed tissue imaging with DNA-conjugated antibodies. *Nat.*  
946 *Protoc.* **16**, 3802–3835 (2021).

- 947 60. Phillips, D. *et al.* Highly Multiplexed Phenotyping of Immunoregulatory Proteins in the  
948 Tumor Microenvironment by CODEX Tissue Imaging. *Front. Immunol.* **12**, 687673 (2021).  
949 61. Goltsev, Y. *et al.* Deep Profiling of Mouse Splenic Architecture with CODEX Multiplexed  
950 Imaging. *Cell* **174**, 968-981.e15 (2018).  
951 62. Sainburg, T., McInnes, L. & Gentner, T. Q. Parametric UMAP embeddings for  
952 representation and semi-supervised learning. Preprint at  
953 <https://doi.org/10.48550/arXiv.2009.12981> (2021).  
954 63. Abhishek Dutta & Andrew Zisserman. The VIA Annotation Software for Images, Audio and  
955 Video. in (ACM, Nice, France, 2019). doi:10.1145/3343031.3350535.  
956 64. Shekarian, T. *et al.* Immunotherapy of glioblastoma explants induces interferon- $\gamma$  responses  
957 and spatial immune cell rearrangements in tumor center, but not periphery.  
958 2022.01.19.474897 Preprint at <https://doi.org/10.1101/2022.01.19.474897> (2022).  
959 65. Bates, D., Mächler, M., Bolker, B. & Walker, S. Fitting Linear Mixed-Effects Models Using  
960 lme4. *J. Stat. Softw.* **67**, 1–48 (2015).  
961 66. Kuznetsova, A., Brockhoff, P. B. & Christensen, R. H. B. lmerTest Package: Tests in Linear  
962 Mixed Effects Models. *J. Stat. Softw.* **82**, 1–26 (2017).  
963  
964



## 965 **Acknowledgements**

966 This research was performed with the support of the Network for Pancreatic Organ donors with  
967 Diabetes (nPOD; RRID:SCR\_014641), a collaborative type 1 diabetes research project supported  
968 by JDRF (nPOD: 5-SRA-2018-557-Q-R) and The Leona M. & Harry B. Helmsley Charitable Trust  
969 (Grant#2018PG-T1D053, G-2108-04793). The content and views expressed are the responsibility  
970 of the authors and do not necessarily reflect the official view of nPOD. Organ Procurement  
971 Organizations (OPO) partnering with nPOD to provide research resources are listed  
972 at <http://www.jdrfnpod.org/for-partners/npod-partners/>. Research reported in this publication  
973 was supported by the National Cancer Institute and National Institute of Allergy and Infectious  
974 Diseases of the National Institutes of Health under Award Numbers K99CA246061,  
975 5U54CA209971-05, 5U2CCA233195-02, 1U2CCA233238-01, 5U2CCA233195-02, 5U01AI101984-09. The  
976 content is solely the responsibility of the authors and does not necessarily represent the official  
977 views of the National Institutes of Health. C.M.S. was supported by the Swiss National Science  
978 Foundation (P300PB\_171189, P400PM\_183915). We like to thank Yury Goltsev, Pauline Chu,  
979 Sarah Black, Gustavo Vazquez, Aviv Hargil (Stanford University), and Irina Kusmartseva (nPOD)  
980 for excellent assistance. We like to thank Dr. Xavier Rovira-Clavé (Stanford University) for critical  
981 comments on the manuscript.

## 982 **Author information**

983 G.L.B curated data, wrote software, and analyzed data. D.P. and C.M.S contributed significantly  
984 to validating the antibody panel and assisted with analysis. S.D., S.S.B, A.Y., H.A.M., G.K.K., N.N.,  
985 S.R., and J.M. assisted with analysis. G.L.B., J.A.B., G.P.N., and P.L.B., conceptualized the study  
986 and wrote the manuscript. All authors have read and approved the final version of the  
987 manuscript.

## 988 **Ethics declarations**

989 P.L.B.: Founder, Halo Biosciences.

990 N.N.: Founder, Halo Biosciences.

991 PLB, NN and GK have filed intellectual property around 4-MU. PLB, NN and GK hold a financial  
992 interest in Halo Biosciences, a company that is developing 4-MU for various indications.

993 G.P.N. has received research grants from Vaxart and Celgene during the course of this work and  
994 has equity in and is a scientific advisory board member of Akoya Biosciences. Akoya Biosciences  
995 makes reagents and instruments that are dependent on licenses from Stanford University.  
996 Stanford University has been granted US patent 9909167, which covers some aspects of the  
997 technology described in this paper.

998 J.A.B.: Board of director for Gilead and CEO and President of Sonoma Biotherapeutics; scientific  
999 advisory boards of Arcus Biotherapeutics and Cimeio Therapeutics; consultant for Rheos  
1000 Medicines, Provention Bio; stockholder in Rheos Medicines, Vir Therapeutics, Arcus  
1001 Biotherapeutics, Solid Biosciences, Celsius Therapeutics; Gilead Sciences, Provention Bio,  
1002 Sonoma Biotherapeutics.

1003 C.M.S.: Scientific advisory board of, stock options in, research funding from Enable Medicine, Inc.